JGR Solid Earth

RESEARCH ARTICLE
10.1029/2019JB018339

Micro-Seismic Monitoring of a Shear Fault Within a Floating Ice Plate

Cédric Lachaud[1,2], David Marsan[1], Maurine Montagnat[2], Jérôme Weiss[3], Ludovic Moreau[3], and Florent Gimbert[2]

[1]Université Savoie Mont-Blanc, CNRS, IRD, IFSTTAR, ISTerre, Chambéry, France, [2]Université Grenoble Alpes, CNRS, IRD, G-INP, IGE, Grenoble, France, [3]Université Grenoble Alpes, CNRS, IRD, IFSTTAR, ISTerre, Grenoble, France

Key Points:
- A micro-seismic monitoring of a fault is setup to monitor its deformation
- Small undetected fractures control the slip and energy budgets of the fault
- Fractures are mostly a by-product of the imposed slip, similarly to swarm-seismicity

Correspondence to:
C. Lachaud,
cedric.lachaud.pro@gmail.com

Citation:
Lachaud, C., Marsan, D., Montagnat, M., Weiss, J., Moreau, L., & Gimbert, F. (2019). Micro-seismic monitoring of a shear fault within a floating ice plate. *Journal of Geophysical Research: Solid Earth*, *124*, 10,444–10,467. https://doi.org/10.1029/2019JB018339

Received 8 JUL 2019
Accepted 10 SEP 2019
Accepted article online 1 OCT 2019
Published online 25 OCT 2019

Abstract The deformation of a circular fault in a thin floating ice plate imposed by a slow rotational displacement is investigated. Temporal changes in shear strength, as a proxy for the resistance of the fault as a whole, are monitored by the torque required to impose a constant displacement rate. Micro-seismic monitoring is used to study the relationship between fault average resistance (torque) and micro-ruptures. The size distribution of ruptures follows a power-law scaling characterized by an unusually high exponent ($b \simeq 3$), characteristic of a deformation driven by small ruptures. In strong contrast to the typical brittle dynamics of crustal faults, an 'apparently aseismic' deformation regime is observed in which small undetected seismic ruptures, below the detection level of the monitoring system, control the slip budget. Most ($\simeq 71\%$) of the detected ruptures are organized in bursts with highly similar waveforms, suggesting that these ruptures are only a passive by-product of apparently aseismic slip events. The seismic signature of this deformation regime has strong similarities with crustal faulting in settings characterized by high temperature and with non-volcanic tremors.

1. Introduction

Laboratory friction experiments, either spring-slider or fault block models (Rosenau et al., 2017), generally analyze slip events that mobilize the whole slip interface, for example by focusing on the precursory phase leading up to these large scale events. They do not reproduce the complex behavior of a natural fault system in which multiple slip events (earthquakes) with very different sizes accommodate the tectonic forcing, in a regime which, at least during the long duration interseismic phase, can be considered stationary. Dieterich, (1972, 1978, 1979a, 1979b) and Rice and Ruina (1983) have developed models, referred to as Rate-and-State friction laws, allowing to interpret complex slip behaviors (Marone, 1998), e.g., slip nucleation prior to rupture. However, although cohesion likely plays a crucial role during the interseismic period by strengthening the fault, e.g., through crack sealing and asperity welding (Muhuri et al., 2003; Tadokoro & Ando, 2002; Tadokoro et al., 1999; Tenthorey & Cox, 2006; Reches, 1999; Renard et al., 2012), its role in restoring fault strength and controlling slip instability is typically ignored in rate-and-state models. Indeed, in these models, the friction coefficient depends only on time and sliding velocity. Fault restrengthening during quasi-stationary contact, or holding-times during which no slip is imposed, is interpreted as an increase in friction through a growth of the surface of contact along asperities. While this simplification is necessary for understanding the fundamental mechanisms at work during slip on a predefined interface, it makes for a non trivial extrapolation to real faults, for which the nucleation and arrest of ruptures is controlled by healing processes competing with weakening mechanisms, as well as other controlling parameters or processes (including fault roughness and scale invariant geometry).

More recently, several recent studies have described micro-failures accompanying the sliding of a fault block model undergoing several stick-slip cycles (e.g., Goebel et al., 2013; Kwiatek et al., 2014; McLaskey et al., 2014; Mclaskey & Yamashita, 2017; Rivière et al., 2018), but they are either limited to short time intervals or have sizes much smaller than the maximum size that characterize slip over the whole interface. The goal of the present work is to extend these recent studies, by experimentally exploring the complexity of ruptures along a fault that naturally formed in an ice plate, and which deforms in a stationary regime not just during macro-ruptures but through a continuum of micro-fractures, like a crustal fault. As will be described in this article, the deformation is here not dominated by the largest slip events, but rather involves a deformation

process for which very small failures, possibly well below the detection limit, contribute significantly to the overall slip budget.

We here describe how this brittle deformation and its characteristics can be monitored and analyzed from a micro-seismic monitoring during an experiment performed at a single, constant slip rate. This will be used as a methodological basis for a subsequent study that will explore how the imposed slip rate impacts the deformation characteristics, e.g., the overall fault strength and the crack rate.

The experimental set-up was described and exploited by Weiss et al. (2016), who documented a systematic dependence of the deformation regime with loading rate, i.e., from an intermittent deformation regime at low rotation rate to a more stable (less intermittent) sliding-like regime at high rotation rate. This transition was interpreted in terms of a competition between damage (local micro-ruptures) and healing. In this set-up, cohesion / healing refers to processes at the micro-scale which cause the (pressure-independent) shear resistance to increase with time, e.g., asperity welding and crack sealing. These processes were shown by Weiss et al. (2016) to be thermal weakening in the case of ice, as fault healing is controlled by refreezing. Because of this healing, the shear resistance can be significant even in presence of a low normal stress.

In the purpose of exploring the deformation regimes of a natural fault that accommodate slip through a wide range of micro to macro-ruptures, this experimental set-up offers interesting advantages: (1) the annular geometry allows sliding over very large distances (up to meters), hence the total imposed slip can be several times the fault's length, implying that the fault goes through several loading/seismic cycles; (2) the fault enters a slowly evolving, quasi steady-state; (3) because of the geometry of the experiment and the boundary conditions applied the normal stress is low, resulting only from geometrical mismatch between the two sides of the fault; (4) a wide range of torque drops is indeed observed, so that a non-periodic, complex deformation is the norm. Similar features have also been obtained for granular systems (e.g., Hartley & Behringer, 2003; Lherminier et al., 2019; Miller et al., 1996), but we here reproduce them for a brittle, cohesive medium.

These experimental conditions share similarities with different crustal faulting settings in which temperature is relatively high, yet brittle fracturing still occurs, but mainly through bursts of small slip events. An example is the transition zone, at the bottom of the seismogenic part of the crust and at the interface between a brittle upper zone at shallow depth and a freely sliding zone at greater depth (Scholz, 1998). This transition is thermally controlled and occurs around 300° C (Scholz, 1998). Within this transition zone, the frictional properties of the fault switch from a velocity weakening to a velocity strengthening regime. Spatial variations in mineralogy, pore-pressure (because of differences in hydrothermal conditions) might also be invoked to explain a mix between stable and unstable slip patches. This results in a fault zone where slip is thought to be regulated by this mix of velocity-strengthening patches (stable sliding / creep) and velocity weakening patches (unstable, seismogenic). An example of such geophysical setting is the central segment of the San Andreas Fault near Parkfield, in particular with the existence of Non-Volcanic-Tremors (NVT) (Gomberg et al., 2016; Nadeau & Dolenc, 2005; Nadeau & Guilhem, 2009; Shelly, 2017). Because of their small amplitude and long duration NVT remain difficult to detect and quantify. Thus, establishing a slip budget during episodes of NVT is an issue. Staudenmaier et al. (2019) proposed to close the slip budget using the frequency-magnitude distribution.

The experiment described here thus provides an opportunity to better characterize the quasi-permanent deformation regime of such systems, i.e., the ruptures properties, how they interact with each other, and the slip partitioning.

The only observable available to Weiss et al. (2016) was a global (i.e., at the scale of the whole fault) torque measurement so that the local, spatially variable, complexity of stress release could not be investigated. Also, the temporal and amplitude resolutions did not allow to distinguish small ruptures: the torque increment measured between two successive time steps results from possible micro-ruptures at different positions, as well as strengthening through healing, without the possibility to distinguish between those processes. This effectively restricted the study to a macroscopic description of the fault deformation, in some ways similar to the observation provided by GPS measurements for real crustal faults.

The focus of our study is thus to further develop the observations of Weiss et al. (2016), by adding a seismic monitoring system (accelerometers). This allows isolating the damage (micro-ruptures) and healing processes, and characterizing their distributions in time, space and size. The manuscript is organized as follows: Section 2 describes the experimental setup and the micro-seismic monitoring. The torque variation and the

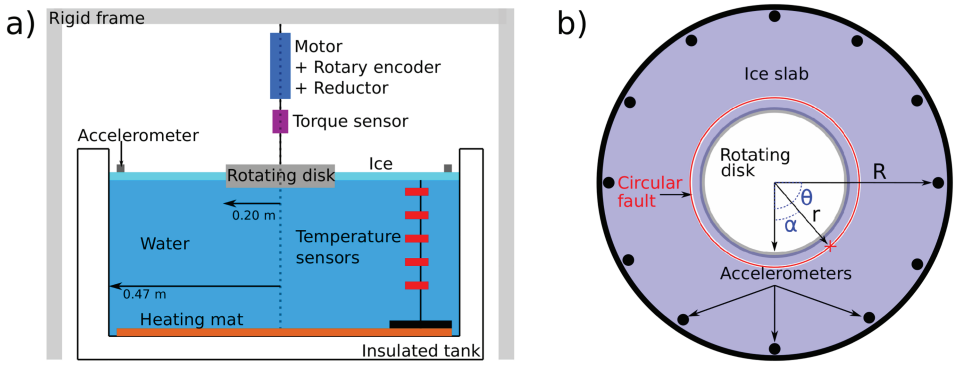

Figure 1. Schematic a) Side-view and b) top-view, of the experimental setup. The fault and accelerometer circle radii are denoted r and R, respectively. α and θ denote a rupture and an accelerometer angular positions, respectively.

seismicity are described in Section 3, where we analyze the rupture size distribution, and investigate how local ruptures occur and interact. The relationship between the observed torque drop and the related rupture magnitude is explored. We also seek to quantify the slip partitioning, between stable and unstable sliding (aseimic/seismic) of this particular fault. These results are discussed in Section 4 in terms of slip processes and seismic coupling and compared with specific crustal systems that share important similarities with our ice fault.

2. Methods

2.1. Experimental Set-Up

The experimental set-up has been designed to imposed a shear deformation along a circular fault within a thin floating ice plate. Its main characteristics are:

1. A circular fault is created by shear failure within an initially undamaged material. This circular geometry allows imposing arbitrary large slip (up to meters) during which fault roughness and properties freely evolve with time.
2. The ice plate thickness is two orders of magnitude smaller than its horizontal extent, so that deformation is localized on a well identified circular fault that can be considered as a 1D object.
3. The relative importance of cohesion-healing and damage can be controlled by varying both the imposed rotational rate and temperature.
4. Given the Couette-like geometry of the experiment with boundary conditions fixed in displacement perpendicularly to the fault plane, no macroscopic normal stress is imposed perpendicular to the fault, although normal stress naturally arises from geometrical mismatch along the fault. Consequently, shear resistance is caused by both cohesion and interlocking of asperities. The importance of one mechanism compared to the other was not investigated. Yet, cohesion is expected to play a dominant role at low rotation rate and low temperature (Weiss et al., 2016).

2.1.1. Shear Deformation Rig

The shear deformation rig used in this study has been described in detail in the study of Weiss et al. (2016). Here, we recall its main characteristics. The shear deformation set-up is built in two parts, cf. Figure 1: (i) a water tank where the ice plate is formed, and (ii) a shear torsion device at the center of the tank.

The circular tank of diameter $d = 0.94$ m and height $h = 0.40$ m was filled with fresh water. The wall was in polycarbonate and was insulated with foam. A circular heating mat (diameter = 990 mm, thickness 3 mm, power = 1 kW) was placed at the bottom and 6 temperature probes (PT100 1/10Din) were used to control and to monitor the water temperature. The regulation of temperature was performed with a PID controller to impose an average temperature of 3.98 ± 0.03°C at the bottom of the tank. The whole set-up was placed in a cold room where the temperature was fixed to -10 ± 0.6° C.

The deformation of the ice-plate was induced by the rotation of a polyoxymethylene disk (diameter = 0.40 m), located at the center of the tank, driven by a brushless servomotor linked to a planetary gear reducer of ratio 1000 and maximal torque 640 N.m. The torque imposed to the ice was measured by a rotary torquemeter (Scaime DR1 1000 N.m) with a precision of 1 N.m. A constant rotation rate of 10 rotations per

day (r.p.d.), equivalent to a sliding rate of 1.6×10^{-4} m.s^{-1} along the fault, was imposed. The servomotor regulation operated at 5 Hz and the torque sampling frequency was 10 Hz.

A circular fault in the ice was created by the rotation of the polyoxymethylene disk. Due to enhanced heat exchange through the polyoxymethylene disk, a small meniscus was observed at the ice/disk interface which shifts the maximum shear stress a few centimeters outward. Consequently, the fault was created at about two centimeters from the inner disk.

The design of the experiment was chosen to apply a shear loading and to allow cohesion-healing. No macroscopic normal stress was applied across the fault, although normal stress can locally build up because of asperity mismatches and water freezing. Dilatancy of the ice gouge was expected to have a minor role because the fault was not vertically confined and gouge material can easily move upward.

2.1.2. Ice Preparation and Characteristics

In this experiment, ice was used as a model material with several advantages. Due to its small shear strength ($\simeq 200-300$kPa estimated from the same shear loading device (Weiss et al., 2016), without clear temperature dependence but a possible weak velocity weakening) and fracture toughness ($\simeq$ 100kPa.m$^{1/2}$; Schulson & Duval, 2009), the formation of the initial fault was easily achieved. Since the experiment was subjected to negative air temperature, water freezing led to cohesion-healing mechanism within the fault. In addition, the ice microstructure can be controlled in order to maximize the microstructural isotropy of the ice. The material was initially homogeneous, with very little heterogeneities and defects.

The ice plate was prepared in order to obtain a spatially uniform thickness of 3mm before the initiation of the fault. To favour isotropy of the polycrystalline ice, water droplets at 0°C are sprayed above the entire surface, creating small nucleation sites that reduce the average crystal size (Weiss et al., 2016). The analysis of thin sections showed that the characteristic grain size is a few centimeters for naturally formed ice crystals, with a strong shape anisotropy. The grain size is reduced to few millimeters with the method described above, with equiaxed grains and isotropic crystallographic fabrics.

While thermal stratification was necessary to avoid localized melting by convection cells, the associated water cooling caused the thickening of the ice plate during the experiment. To estimate the ice thickening rate, thickness was measured on a hourly basis at multiple locations of the plate by drilling holes through the ice during dedicated tests. The thickening rate observed for an air temperature of $-10°C$ was $\simeq$ 1 mm/hour and was constant throughout the experiment duration (5 hours). This growth rate was consistent with the 1D thickening model used by Weiss et al. (2016). Also, before the initiation of the fault, no measurable thickness spatial variation could be identified. At the end of the experiment, a difference in thickness between the ice close to the fault and the ice far from it was noted, 4 mm and 8 mm respectively. Enhanced thermodynamic fluxes along the fault could explain this thickness difference. Moreover, due to fault damage and re-freezing along the fault, the ice thickness within the fault was not known with precision. In this study, a constant thickness was assumed to calculate the rupture size (see section 3.2).

Ice Ih deforms in a brittle (see ; Schulson, 2001for a review) or ductile manner (Glen, 1955; Goldsby & Kohlstedt, 2001; Schulson & Duval, 2009), depending on the strain rate and temperature. At the tested rotation rate, i.e., 10 r.p.d, the equivalent strain rate for an average fault width $\lambda \simeq 1$ cm (this corresponds to an average value with variations observed in space and time), a driving rate $\Omega = 10$ rpd and a fault radius $r_f \simeq 0.22$ m is $\dot{\gamma} = \frac{\Omega r_f}{\lambda} \simeq 2.5 \times 10^{-3}$ s^{-1}. This value is orders of magnitude larger than the ductile-brittle transition strain-rate of ice at -10° C under tension, 4×10^{-7} s^{-1} for a grain size of 1 mm, and under compression, 8×10^{-5} s^{-1} for a grain size of 6 mm (under no confinement), at temperatures similar to that study (Schulson & Duval, 2009). Because of the dependence of the ductile-to-brittle transition strain rate to grain size, $d^{-3/2}$ (Batto & Schulson, 1993; Schulson & Duval, 2009), creep could be observed at temperature lower than temperature used in this study for smaller grains (Caswell et al., 2015). In addition, ductile deformation (creep) of polycrystalline ice is a velocity-strengthening process (e.g., Duval et al., 1983), in strong contrast with the fault deformation process in our experiment, which is velocity-weakening (Weiss et al., 2016). Fortt and Schulson (2007) carried out friction experiments along shear faults in ice. A velocity strengthening regime, interpreted as resulting from ductile deformation of bulk ice (supported by ; Barnes et al., 1971), was observed for sliding rates below 8×10^{-6} m.s^{-1} which corresponds to a transition between ductile and brittle processes. Above this transition, brittle deformation as well as localized melting appeared. The rotation rate of the experiment described here (10 r.p.d) corresponds to a sliding velocity of 1.6×10^{-4} m.s^{-1}, much larger than this transition velocity. Candela and Brodsky (2015) argue that for asperities under a critical size

L_c, e.g., varying from 4 μm to 500μm on natural faults, the deformation does not occurs by elastic shearing but could instead occurs by plastic yielding. This critical length scale is supposed to vary with the material hardness (that is varying with temperature and strain rate in ice ; Barnes & Tabor, 1966; Poirier et al., 2011) and Young modulus.

Weiss and Schulson (2000) have shown that Grain Boundary Sliding (GBS) is a linear viscous process, hence neither velocity-strengthening, nor velocity weakening unlike the fault deformation process of our experiment (Weiss et al., 2016).

Possible lubricating effect due to liquid water was not investigated in our study. Frictional heating, even in combination with pressure-melting is likely insufficient to melt the surface (Schulson & Fortt, 2012).

Based on these considerations, we can conclude that, although ductile deformation processes might locally play a role in our experiment, sliding and deformation along the fault is essentially accounted for by brittle ruptures.

2.2. Micro-Seismic Measurements

An array of 12 vertical accelerometers (Bruël and Kjaer type 4393-v, mounted resonance frequency of 75 kHz) was used to perform two types of experiment. Speed and attenuation of the waves propagating in the ice sheet were measured by setting the sensors in line on an undeformed ice plate. The aim was to determine the dispersion curves of the propagating waves in order to characterize the wave modes that were present. Then, the accelerometers were set with regular spacing along a circle around the fault to monitor ice rupture during faulting (Figure 1). These accelerometers were connected to conditioning and amplifier devices (Bruël and Kjaer Nexus type 2692-0S4), and acquisition was carried out by a General Standard card PCI-express 66-16AISSA0. A full-waveform acquisition was performed at a sampling frequency of 500 kHz. The signal was band-pass filtered between 10 kHz and 65 kHz, hence avoiding spurious effect related to the resonance frequency at 75 kHz of the sensors.

2.2.1. Waves and Attenuation

Propagation of elastic waves in plates was first theorized by Rayleigh (1888) and Lamb (1917). For a 2D plate in a vacuum, there exist three fundamental modes: a symmetric mode, referred to as S0, an anti-symmetric mode, referred to as A0, and a symmetric transverse SH mode.

For frequencies typically less than 100 kHz and for a minimum ice thickness of 3 mm, the S0 mode is mainly non-dispersive, and corresponds to longitudinal waves with mostly radial displacement propagating at $V_L = 2\frac{\beta}{\alpha}\sqrt{\alpha^2 - \beta^2}$, where α and β are the velocities of P and S waves in ice. Unlike this S0 mode, the A0 mode is always dispersive, even at low frequencies, i.e., for f on the order of a few kHz (and for a minimum ice thickness of 3 mm). In that case, the group velocity V_G, can be described as $V_G = 2 \times 3^{-1/4}\sqrt{\pi H V_L f}$ where H is the ice thickness. Finally, the SH mode is a transverse horizontal displacement propagating non-dispersively with velocity β. Other, higher modes exist, but are expected to only affect high frequencies, typically greater than 100 kHz for $H = 3$mm. Since we filter out these high frequencies, these modes will be ignored.

Press and Ewing (1951) described later the various modes of propagation of elastic waves in a floating ice sheet. Neglecting gravity and replacing atmosphere by vacuum, they showed that solutions cannot be reduced to the classical symmetric and anti-symmetric modes, as expected given the non-symmetrical geometry of the problem. Yet, compared to Lamb's modes, related modes exist, and in what follows we will refer to those as quasi-symmetric, QS0, and quasi-anti-symmetric, QA0.

In a previous experimental work on wave propagation modes, using the very same set-up and accelerometers, we demonstrated that QS0 and QA0 modes are found as expected, on top of a slower Stoneley (or quasi-Scholte) mode propagating along the ice-water surface (Moreau et al., 2017). The SH mode was absent likely because we recorded the vertical acceleration only.

In addition to the work done by Moreau et al. (2017), new experiments were conducted to characterize the propagation velocities and the attenuation of these modes for the specific needs of the present study. Accelerometers were linearly arranged and spaced by 5cm away from each other. Hsu-Nielsen sources (pencil-lead break) were used as experimental sources.

Figure 2 shows the waveforms recorded at several distances from the source for 3mm and 9mm thick ice plates. The velocity of the observed QS0 mode is similar to that predicted when neglecting the presence

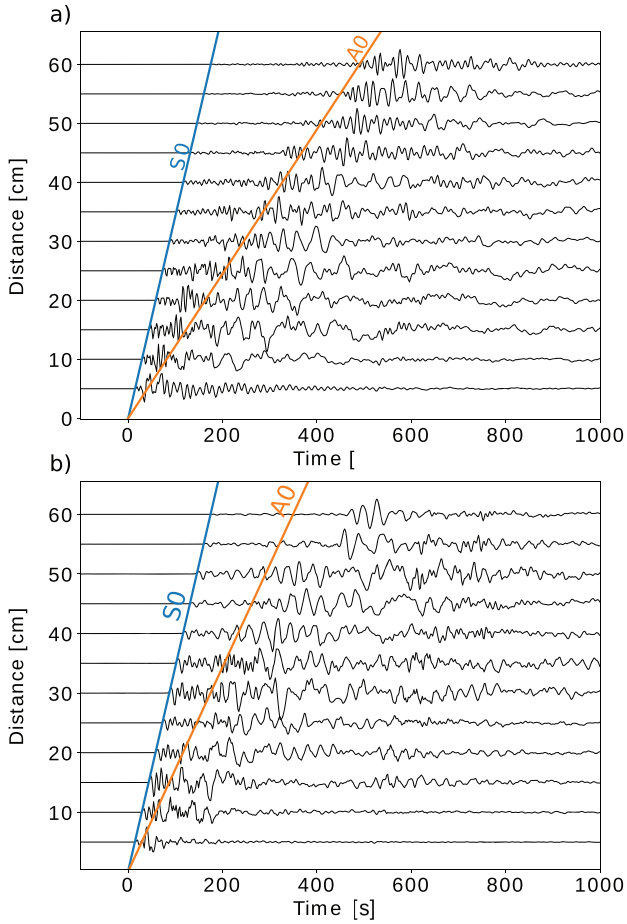

Figure 2. Normalized waveforms recorded at different distances from the source for a floating ice plate of thickness a) 3 mm and b) 9 mm. The source is of Nielsen-Hsu type, which is commonly used in acoustic-emission testing. Lines refer to the theoretical S0 (blue) and A0 (orange) propagation modes in vacuum. The origin time $t = 0$s is the time of the source.

of water underneath. S0 theoretical wave velocities are 3427 m.s^{-1} and 3428 m.s^{-1} (blue vertical lines on Figure 2) for a thick plate in vacuum with respectively 3 mm and 9 mm thickness. For the same thicknesses, experimentally-estimated velocities of QS0 are 3387 m.s^{-1} and 3399 m.s^{-1}. The flexural mode was, as expected, significantly affected by the presence of water. The predicted A0 wave group velocities were 1432 m.s^{-1} and 1849 m.s^{-1} for 3 mm and 9 mm thick ice plates respectively, while the measured group velocities were 1202 m.s^{-1} and 1275 m.s^{-1}, respectively.

The amplitude of the QS0 mode were manually picked using the maximum of the envelope in the time interval defined between the QS0 and QA0 arrivals. At the distances and frequencies investigated here, the amplitude of QS0 scaled as $A(x) \propto x^{-m}$ with x the distance from the source, cf. Figure 3. Attenuation increased with ice thickening, likely due to an increase in anelastic attenuation. For a 3 mm thick ice plate, an exponent $m = 0.98$ was obtained by linear regression, for a 9 mm thick plate the value of the exponent was $m = 1.46$. For an elastic plate in vacuum, with only a 2D geometrical attenuation of the signal, a value of $m = 1$ is expected.

Hereinafter, the QS0 phase will be used to characterize the micro-ruptures. Indeed, it was (1) the first phase to reach the sensors, (2) non-dispersive, and (3) of lower amplitude than the QA0 phase (because vertical acceleration was recorded), enabling us to quantify the wave amplitude even for the largest sources for which the QA0 phase saturates.

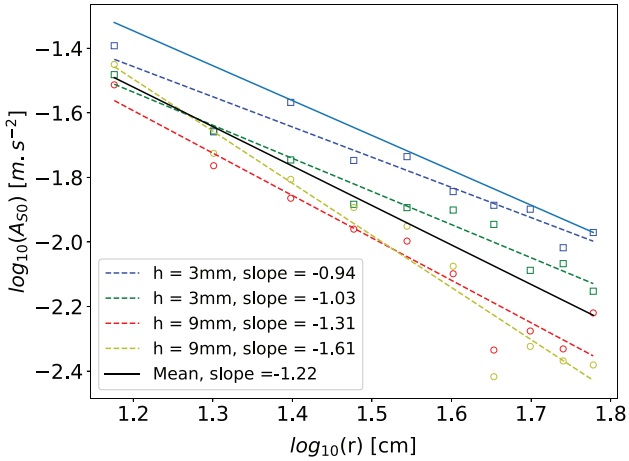

Figure 3. Maximum amplitude of the QS0 mode, A_{S0}, as observed experimentally as a function of the distance to the source, r, for a 3 mm (squares) and 9 mm (circles) thick ice. Dashed-lines are the best linear fits for each data-set and the solid line is the best fit of all data-points.

2.2.2. Micro-Seismic Monitoring

Ruptures occur during the experiment, marking the deformation of the ice plate. These events were localized along the fault and their seismic moments were computed using the full waveforms recorded with the 12 accelerometers (described in section 2.2). To monitor the fault deformation, the array was designed as a 45 cm-radius circle with regular spacing of 30° between two accelerometers. Those were settled at distance from the fault to maximize the arrival time differences between them.

We detail below how these ruptures were detected and localized based on seismological techniques that were adapted to our experimental scale and geometry. Event detection was performed automatically using a STA/LTA algorithm (cf. Allen, 1982; Vanderkulk et al., 1965). This method compares the average amplitude computed over a short time window, referred to as STA, with the average amplitude computed over a longer time window, referred to as LTA and representing the background amplitude. The STA and LTA durations were empirically determined in order to maximize the sensitivity to the targeted seismic signals while minimizing the number of false detections; we use 20 μs and 200 μs for the STA and LTA, respectively. The best threshold, STA/LTA=8, was estimated in order to get zero false triggering on a set of 20 events randomly chosen in a set of 100 detections. The *classic-sta-lta* algorithm of the Python *obspy* library (Beyreuther et al., 2010) was used. An improved arrival picking was performed an detected event based on the Kurtosis, K, of the signal (Saragiotis et al., 2002). The Kurtosis was used to identify the transition between a Gaussian noise and non-Gaussian waveforms. The Kurtosis was computed over a running window of length 0.2ms, after filtering in the 10 - 65 kHz bandwidth. When K exceeded a threshold value of 10 the corresponding time was taken as the arrival time of the QS0 mode. The Kurtosis threshold was determined empirically to limit false detection and increase the accuracy of the picking.

Given that only one circular fault of 22 cm-radius was formed, it was assumed that all the detected ruptures were localized in or very close to the fault, so that event location only required solving for the angular position. To locate the ruptures, a two-step method was settled. In the first step, a first estimate was obtained using the QS0 arrival times picked by the Kurtosis. In the second step, whenever it was possible, this estimation was improved by determining the arrival time difference between similar waveforms (i.e., distinct but similarly-looking sources), and compute refined, relative locations for a whole group of such similar events (referred to as multiplets, e.g., Got et al., 1994).

A multiplet is defined as a set of ruptures having at least 95% coherency with each other measured at two accelerometers or more. Relocation was performed with respect to the multiplet barycentre, defined as the average of the locations estimated by kurtosis. For this relocation, relative time delays between two waveforms measured at the same accelerometer were computed using both cross-correlation and coherency on 1ms long windows. To avoid outliers, when their difference was larger than 5 μs the two estimates were discarded (corresponding to an error of 17mm for waves propagating at 3400m.s^{-1}). If both estimates lead to similar results (i.e., their difference was less than 5 μs), then the average of those time delays was used.

Assuming that the multiplet size is small compared to its distance to the accelerometer, the distances of each event in the multiplet to this accelerometer are nearly identical. The positions of the ruptures relative to the barycentre were computed by linearizing the problem, which allows for a quick and robust inversion.

The radii of the fault and of the circle of accelerometers positions are $r = 22$ cm and $R = 45$ cm respectively. The angular position of rupture B, with A and B two ruptures with similar waveforms, is denoted by α_A with $\alpha_A + \phi$ (with $\phi \ll 1$). Denoting θ_i the angular position of an accelerometer i, the distances of A and B to the accelerometer are

$$d_B = d_A + \frac{Rr\phi}{d_A}\sin(\alpha_A - \theta_i). \tag{1}$$

The difference in waves travel times is then

$$\Delta t_i = \frac{Rr\sin(\alpha_A - \theta_i)}{Vd_A}\phi = \tau_i\phi, \tag{2}$$

where V is the velocity of the QS0 mode, and time τ_i is a parameter that can be approximated for the whole multiplet as $\tau = \frac{Rr\sin(\overline{\alpha}-\theta_i)}{V\overline{d}}$ where $\overline{\alpha}$ and $\overline{d}$ relate to the barycentre position of the multiplet. So, still for events A and B and accelerometers i and j, the theoretical double difference of travel times, denoted $\widehat{\Delta t}_{i,j}^{(A,B)}$, is:

$$\widehat{\Delta t}_{i,j}^{(A,B)} = \Delta t_j^{(A,B)} - \Delta t_i^{(A,B)} = (\tau_j - \tau_i)(\phi_B - \phi_A) \tag{3}$$

with $\phi_A = \alpha_A - \overline{\alpha}$. Knowing the observed double differences $\Delta t_{i,j}^{(A,B)}$, we compute the angles ϕ for all the ruptures in a multiplet by minimizing the quadratic cost function J:

$$J = \sum_{\substack{i,j \\ A,B}} \left((\tau_j - \tau_i)(\phi_B - \phi_A) - \Delta t_{i,j}^{(A,B)}\right)^2 \tag{4}$$

For each event A in a multiplet, we look at all the other events $B, C, \ldots$, that share at least two time delays at different sensors. We then define for each pair $AB, AC, \ldots$, the sets $S_{AB}, S_{BC}, \ldots$, of sensors that relate to these time delays. Finally, we define $S_A, \ldots$, as $S_A = \{S_{AB}, S_{AC}, \ldots\}$, a list of (possibly repeating) sensor indexes. For example, if A and B share time delays at sensors 1,2 and 3, and A and C at sensors 2 and 3, then:

$$\begin{aligned} S_{AB} &= \{1, 2, 3\}, \\ S_{AC} &= \{2, 3\}, \\ S_A &= \{1, 2, 2, 3, 3\}. \end{aligned} \tag{5}$$

Minimizing J with respect to $\underline{\phi} = {}^t(\phi_A \quad \phi_B \quad \ldots)$ then leads to the solution

$$\underline{\phi} = \underline{\underline{M}}^{-1}\underline{\Delta} \tag{6}$$

where $\underline{\Delta}$ is the column-vector containing all the time differences, e.g., $\underline{\Delta} = {}^t(\Delta t_{1,2}^{(A,B)} \quad \Delta t_{2,3}^{(A,B)} \quad \Delta t_{2,3}^{(A,C)})$ in our example just above, and $\underline{\underline{M}}$ is a symmetric matrix $\{M_{AB}\}$ such that:

$$\begin{aligned} M_{AA} &= -\Sigma_{S_A}(\tau_j - \tau_i)^2 \\ M_{AB} &= -\Sigma_{S_{AB}}(\tau_j - \tau_i)^2 \end{aligned} \tag{7}$$

For a multiplet with N ruptures, it can be shown that $\underline{\underline{M}}$ has a rank equal to $N - 1$. We therefore estimate $\underline{\phi}$ using equation (6) for $N - 1$ events and relocate the last event by imposing that the mean of all N deviation angles ϕ is zero (this amounts to constraining the barycenter of all the relocated ruptures to be effectively located at the angular position α).

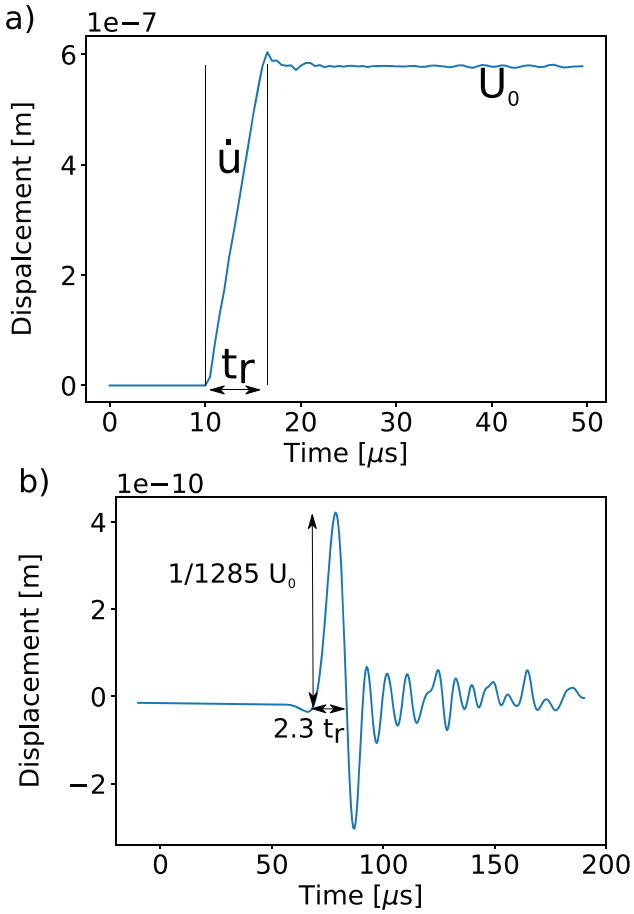

Figure 4. Far-field displacement due to a shear dislocation modelled using the COMSOL software. a) Horizontal displacement U_0 imposed on the rupture defined as a 1cm × 1cm dislocation, with rupture velocity $V_r = 1675$ m.s^{-1}, sliding velocity $\dot{u} = 0.1$ m.s^{-1} and rupture duration t_r. b) Vertical displacement modelled at a distance $r = 0.25$m from the source.

2.3. Quantifying Seismic Moment and Magnitude

To characterize the rupture size, we aim at computing its moment magnitude, M_w, through the estimation of the seismic moment $M_0 = \mu ULW$ (Aki, 1966; Kanamori & Anderson, 1975), where μ is the shear modulus of ice, equal to 3.52 GPa (Schulson & Duval, 2009), U the average displacement (slip) along the rupture, L and W the rupture length and width, respectively. Our approach consists in (i) determining L directly from temporal characteristics of the recorded signal (i.e., first zero-crossing time; and/or duration of the source time function), and (ii) estimating U, the horizontal displacement, from the vertical maximum displacement at the sensors using a finite element method (COMSOL software, www.comsol.fr).

The displacement field induced by a pure shear failure on a rectangular asperity with no cohesion have been model. The rupture was modelled as a displacement U_0 between two parallel vertical surfaces of length L and width W. The asperity width was set equal to the plate thickness. The rupture velocity for earthquakes typically ranges between 0.6 and 0.9 times the shear wave velocity (Heaton, 1990; Madariaga, 1976). In this study, the rupture velocity was defined as $V_r = 0.9V_{Rayleigh} = 1675$ m.s^{-1}. The rupture growth and propagation were not modelled, and impose the displacement to be uniform over the dislocation, evolving in time as a ramp function $u(t) = \dot{u}t$ for $t_0 < t < t_0 + t_r$, with $\dot{u}$ the sliding velocity, t_0 the time of rupture onset and $t_r = L/V_r$ the duration of the rupture. Please not that, in this approach, V_r is not a true rupture velocity, since our dislocation slips at once (so effectively at an infinite rupture velocity); however, V_r constrains the rupture duration t_r. Figure 4.a shows the observed horizontal source displacement as a function of time. At any time $\delta t = t - t_0$ during the rupture, the total moment is $M_0(t) = \mu u(t)LW = \mu\dot{u}\delta tLW$. The total displacement is $U_0 = \dot{u}\frac{L}{V_r}$, related to the moment rate $\dot{M}_0 = \mu\dot{u}LW = \mu U_0\frac{W}{V_r}$. For given μ, W and V_r, our

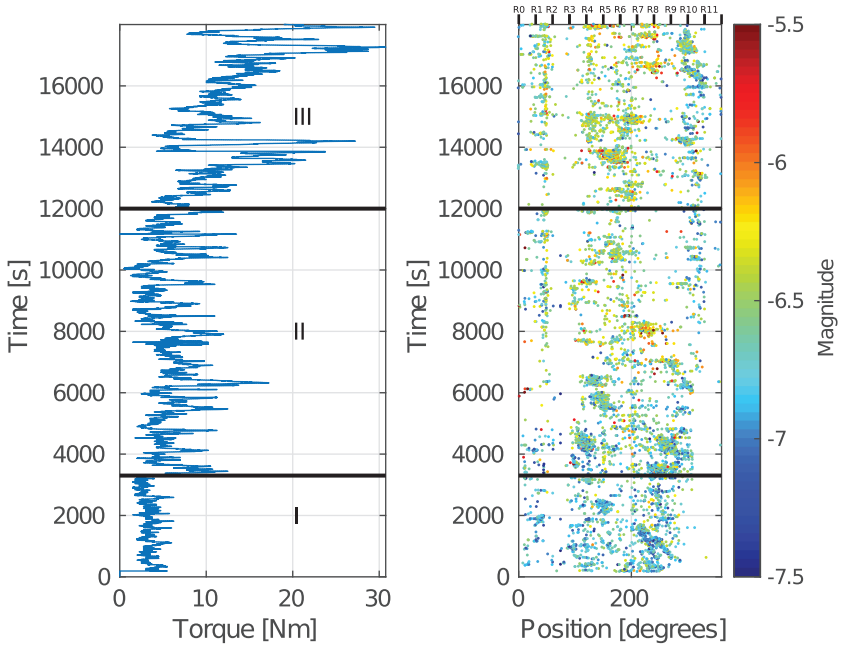

Figure 5. Left: Torque measured for the imposed velocity of 1.6×10^{-4}m.s^{-1} at $-10°C$. The initial rupture that creates the fault is not shown, t_0 represents the time immediately after this rupture. Right: Space and time distribution of the detected ruptures. The color scale represents the magnitude. R0, R1, … , R11 labels represent the accelerometers positions.

model considers that $\dot{M}_0$ is directly proportional to U_0. From the duration and peak amplitude of the first QS0 pulse both the rupture length L and the displacement U_0 can be estimated, as detailed below.

In our analysis, QS0 half-period, noted as $T_{1/2}$, was used as a proxy for the QS0 pulse duration to estimate the rupture length which is proportional to the rupture duration. Since the QS0 mode can be considered as non-dispersive at the studied frequencies, the QS0 half-period is proportional to the duration of the first displacement pulse. Based on our model, it was found that the pulse duration scales as $t_r = 0.43T_{1/2}$ (the pre-factor varying from 0.41 to 0.45), cf. Figure 4.b. The estimated rupture lengths of the detected ruptures were in the 7×10^{-2} to 4×10^{-1}m range, with an average of 7×10^{-2}m. The observed rupture length were larger than the fault width ($L > W$) so our assumption that the rupture breaks the whole thickness was reasonable.

Numerical modeling yields a constant ratio between the horizontal displacement at the source and the vertical displacement at distance $r = 0.25$m averaged over 3 sensors equal to $U_0/U_{z,r} = 1285 \pm 64$, cf. Figure 4.b. Using this proportionality the source displacement was estimated to vary between 9×10^{-10}m and 2×10^{-5}m. The 10th and 90th percentiles are 4×10^{-8}m and 3×10^{-7}m, with a median value of 1×10^{-7}m.

Seismic moments were found to range from 1.7×10^{-3}N.m to 3.5×10^{1}N.m, corresponding to moment magnitudes between -7.9 and -5.0. These magnitudes appear very small, but are in agreement with the magnitude of microfracturing events measured in lab experiments (Bohnhoff et al., 2009; Goodfellow & Young, 2014; McLaskey et al., 2014; McLaskey et al., 2015). The frequency-magnitude distribution of the ruptures is discussed in Section 3.2 in reference to the Gutenberg-Richter law.

3. Results

Our aim is to analyze how the numerous ruptures contribute to the overall deformation of the ice plate, and how these ruptures are distributed in space, time and energy. We start by a qualitative description of the torque and rupture rate time series, and then perform a statistical description of the seismicity.

3.1. Global Torque and Seismicity Characteristics

We first investigate the links between torque and seismicity at the global scale. The torque time series, after the initial rupture that creates the circular fault, is shown in Figure 5.a. The initial ice plate strength just

Table 1
Average Torque (± the Standard Deviation) and Coefficient of Variation for the Three Different Phases in the Torque Time Series

Phase	I	II	III
Average Torque (N.m)	3.1 ± 1.1	5.9 ± 2.5	12.5 ± 5.2
$\sigma(\Gamma)/ < \Gamma >$	0.37	0.43	0.41

before this rupture is about 400 N.m, which is consistent with the values obtained by Weiss et al. (2016), and much larger than the fault strength, as the maximum torque value afterwards is $\Gamma = 31$N.m. Spring-slider experiments typically display either stick-slip or stable sliding, i.e., all interface asperities collectively accumulate stress or fail together (see Marone, 1998 for review). In the absence of an experimentally imposed normal stress, the equivalent interface shear stiffness of our fault is too weak to produce this simple stick-slip dynamics. Instead, we observe a complex mix of local ruptures and local recovery / stress accumulation, akin to the complex behaviour of a fault system. An overall positive trend of the torque with time is observed associated with a thickening of the ice plate. Based on average torque, three different phases can be distinguished; from 0 to 3000 s, from 3000 s to 12000 s and from 12000 s to the end of the experiment. Average torque and normalized standard deviation $\sigma(\Gamma)/ < \Gamma >$ (i.e., coefficient of variation) are given in Table 1. The fluctuations simply scale with $< \Gamma >$, i.e., the coefficient of variation remains constant throughout the phases.

The torque and seismicity time series are compared by synchronizing the two clocks by minimizing the time delays between the 10 largest torque drops and the 10 largest ruptures. We detected 24938 ruptures after the formation of the fault, with 1381 multiplets which represent 71% of all ruptures. All multiplets have been relocated using the double difference method described above (see Section 2.2.2). Figure 5.b shows the space-time distribution of the ruptures and their clustering.

The rupture rate varies from 0 to 63 ruptures per second, cf Figure 6. The rupture rate is intermittent, and, in comparison to the torque time series, does not show clear changes in behaviour over time, i.e., phases I to III observed in Figure 5 are absent in Figure 6. The cross-correlation between torque drops and rupture rate is extremely small (value=0.025). Yet, computing a cross-correlation on 500 s-long time windows shifted sample by sample, we observe an average cross-correlation of 0.05, further increasing in phase III with cross-correlation values up to 0.35 associated to the large torque drops.

3.2. Characterizing the Rupture Size Distribution

To describe the observed seismicity along the fault, we looked at the frequency-magnitude distribution of ruptures. Since the ice thickness was not precisely monitored during the experiment (see section 2.1.2), we

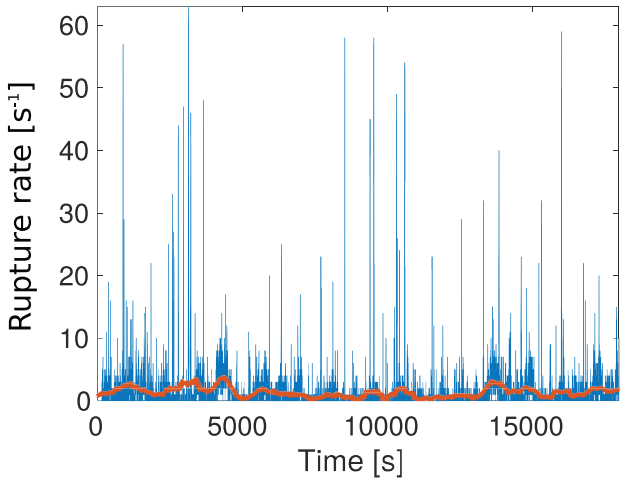

Figure 6. Rupture rate function of time computed for a 1 s-long time step. The orange curve is the 600 s-long moving average.

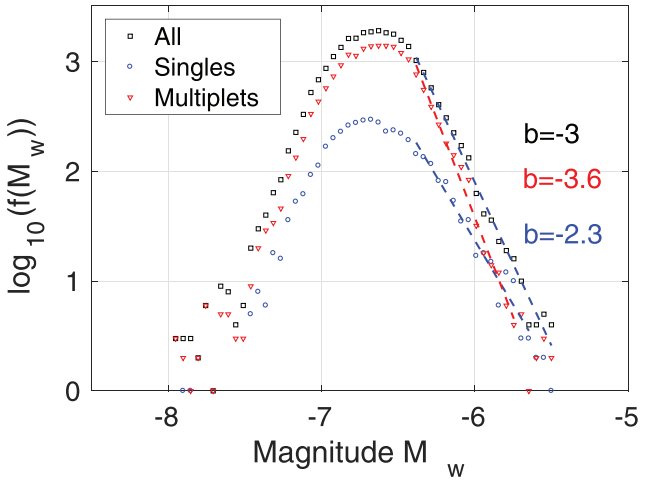

Figure 7. Probability density function of the relative magnitude, M_w, (symbols) and the best linear fits (dashed lines) taking into account all the ruptures (black), ruptures not included in a multiplet only (blue) and ruptures in a multiplet only (red).

assumed a constant ice thickness of 6 mm. It corresponds to the average between the initial and final plate thickness.

The moment magnitudes (M_w) of the detected ruptures vary between −7.9 and −5. The distribution of M_w is investigated by considering three different populations, taking into account (i) all ruptures, (ii) only multiplets and (iii) only ruptures not included in a multiplet (see Figure 7). Multiplets represent 71% of all ruptures, which explains why the first two probability density functions are similar. For the three populations, the density is maximum near $M_w = -6.6$. We checked that a less sensitive detection, i.e., with a higher STA/LTA threshold, shifts this mode to higher M_w values. The estimated completeness magnitude of our detection method is $M_w = -6.4$. For higher magnitudes, a power law decrease of the density of ruptures with magnitude is observed following, $f(M_w) = 10^{-bM_w}$. This decrease goes as $f(M_w) \propto 10^{-3.0M_w}$ when considering all ruptures, $f(M_w) \propto 10^{-3.6M_w}$ when considering multiplets, and $f(M_w) \propto 10^{-2.3M_w}$ when considering only isolated ruptures. The large b-values observed imply a small dispersion of the magnitudes. In the three cases, the b-value is much higher than for crustal earthquakes, for which b is generally close to 1 (Utsu, 2002). As discussed in Section 4.2, this has important consequences on the characterization of the fault deformation.

The multiplets represent a large part of the detected events and are related to a specific deformation dynamics. To get a more detailed view of the multiplet population, we analyze the variability in rupture moments of the 100 larger multiplets. These groups contain between 30 and 765 ruptures for a total of 10259 ruptures (41% of all the ruptures and 58% of the multiplets). Multiplets display different M_w statistics than non-multiplets, as shown in Figure 8. Since they correspond to the rapid occurrence of close-by or even repeating ruptures, it can be expected that the magnitudes of the ruptures within a multiplet tend to be characteristic (i.e., repeated breaking of a single or a limited set of asperities). Indeed, the standard deviation of the seismic moment of ruptures not included in a multiplet and the average standard deviation of the seismic moment of each individual multiplet are $\sigma(M_0) = 1.3$ and $\sigma(M_0) = 0.21$, respectively. To compare these distributions with respect to a Gaussian distribution we compute the skewness ζ and Kurtosis K, which measure the distribution tail asymmetry (ζ) and the excess of outliers compared to the normal distribution (K); they are equal to 0 and 3 for a Gaussian, respectively. The averages of ζ and K values for all the multiplets are 2 and 5, while these values are 15 and 280 for ruptures not in multiplets. This clearly indicates that rupture size in a multiplet tends to have a limited variability as is it visible in Figure 8 that shown the histograms of the seismic moments for the multiplets and non-multiplets ruptures.

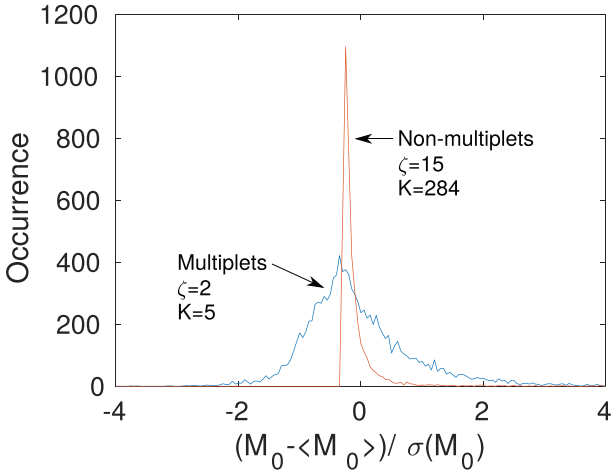

Figure 8. Histograms of rupture seismic moments normalized by the mean and standard deviation. For ruptures not included in a multiplet (red), the mean $< M_0 >$ and standard deviation $\sigma(M_0)$ are calculated over all non-multiplet events. For ruptures included in multiplets (blue), the mean and standard deviation are computed individually for each multiplet. ζ is the skewness of the distribution and K the kurtosis.

As a summary, the frequency magnitude distribution of the ruptures exhibits a power-law distribution similar to a Gutenberg-Richter law with a b-value of about 3, much larger than what is usually observed for crustal faults. In addition, we identify two populations of ruptures, one composed of unique events, the second composed of multiplets, i.e., ruptures with highly similar waveforms, that display a characteristic size, each multiplet having its own characteristic magnitude.

3.3. Clustering in Time and Space, and Triggering

We now characterize the dynamics of the deformation along the fault as seen from the temporal and spatial distribution of the ruptures.

3.3.1. Time Clustering of the Ruptures

To characterize the distribution in time of the rupture events, we compute the correlation integral, defined as (Grassberger & Procaccia, 1983):

$$C(\Delta t) = \frac{2}{N(N-1)} N(\delta t < \Delta t) \quad (8)$$

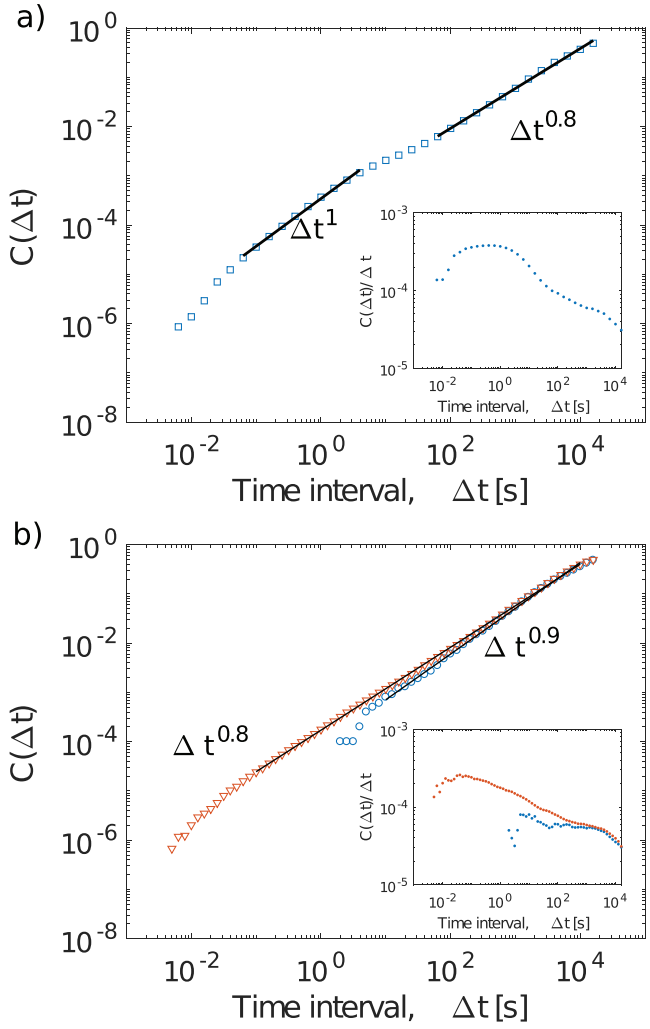

Figure 9. Correlation integral in time, $C(\Delta t)$, computed by considering a) all the detected ruptures, b) each multiplet as a single event, taking the mean occurrence time as its occurrence time. In b), we distinguish two populations: (blue) only the multiplets, (red) multiplets and independent (isolated) ruptures not in multiplets. The time resolution of the detection is 3.6 ms and the duration of the experiment is 5 hours. The insets show $C(\Delta t)/\Delta t$.

where $N(\delta t < \Delta t)$ is the number of ruptures such that δt, the time separation between two ruptures, is less than the time lag Δt, cf. Figure 9.a. Two different regimes are observed: for time interval less than a few seconds the power-law exponent of the correlation integral, i.e., the correlation dimension δ, is close to one, implying that the ruptures are randomly distributed. This regime does not result from a lack of resolution since the detection method allows for the detection of time intervals between ruptures as low as 4 ms. This $\delta = 1$ value is characteristics of the dynamics within multiplets: during the activation of a multiplet, occurring at time scales less than about 10 s, the rupture occurrence times are evenly distributed with no short-time scale clustering. This homogeneous distribution at time scales less than 10 s suggests that the ruptures do not trigger each other. At longer time scales we observe $\delta = 0.8$, hence (weak) clustering in time, i.e., damage is intermittent.

To explore the clustering beyond the simple short-term homogeneity within multiplets, we consider multiplets as single events and define their occurrence time as the mean of the occurrence times of the individual ruptures they include. The correlation integral (Figure 9.b) shows that (1) taking into account only the multiplets, a power-law develops from a few seconds (median duration of the multiplets) to the duration of the experiment, with a correlation dimension equal to 0.9, i.e., ruptures are close to a Poisson process although some weak clustering exists; (2) taking into account multiplets and the independent ruptures, we recover the power-law regime with $\delta = 0.8$, that now extends down to short time scales. This shows that the time

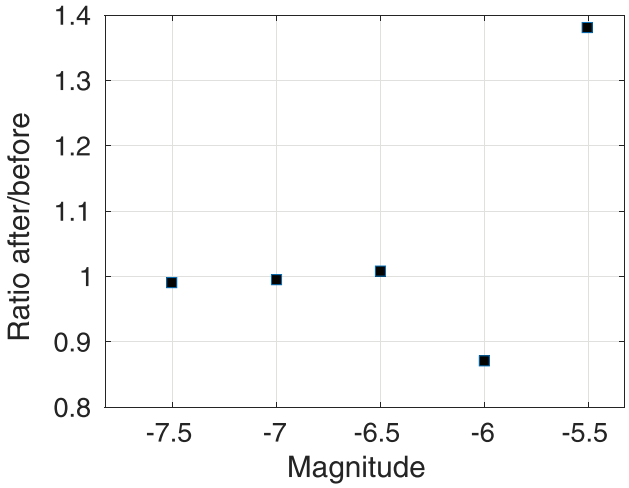

Figure 10. Ratio of the average number of ruptures after the 'main-rupture' by the average number of ruptures before (± 1 s). Each rupture of the given magnitude range is considered successively as the 'main-rupture'.

series is made of two superimposed components: weak clustering from the time resolution (about 4 ms) to the integral scale (hours), and occurrence times homogeneously distributed within multiplets that dominate the correlation integral up to the typical duration of multiplets (about 10 s).

Potential triggering of a sequence of ruptures by a previous rupture is investigated. To do so ruptures are grouped in magnitude intervals, from −7.5 to −5.5. Figure 10 shows the ratio between the average number of ruptures occurring after any given rupture, consider as the “main-rupture”(as in “main-shock”), and the average number of ruptures occurring before, for a time interval of ± 1 s. For the largest magnitude interval [−5.5, −5], we observe 38% more rupture occurring after than before the main-rupture, implying that even the largest ruptures trigger only a small number of “after-ruptures”. For main-ruptures of magnitude $M_w \in [-7.5, -5.5]$, the ratio only weakly departs from the value of 1, implying no triggering. This is very different from crustal seismicity, which typically exhibits strong triggering in the form of aftershock sequences that can last for years.

This analysis is complemented by stacking the cumulative number of ruptures in a ±0.5 s interval around large main-ruptures (with $M_w \in [-5.5, -5]$), cf. Figure 11. A significant increase in rate is seen within the few tenths of second, from about 3.7 ruptures per second to 11.5 ruptures per second. In addition, within the time interval investigated, the post rupture rate remains higher than the pre-rupture rate.

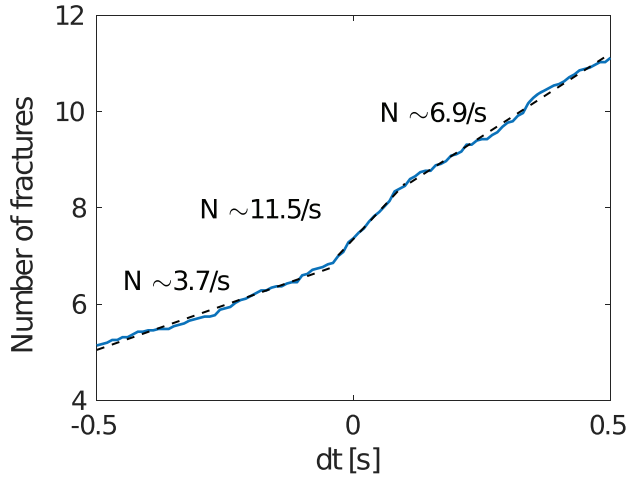

Figure 11. Average cumulative number of ruptures for magnitude $M_w \in [-5.5, -5]$. Dashed black lines are the best linear fits on selected time intervals. The time t=0 s is the time of the “main-rupture”.

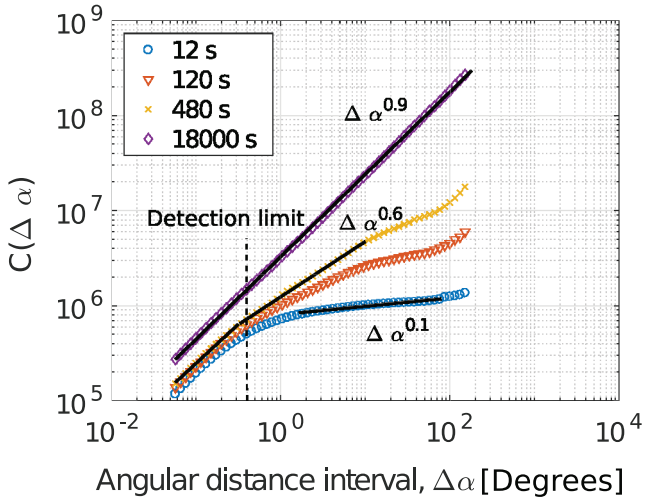

Figure 12. Correlation integral in space (angular separation) for several time interval conditions. The black lines show the power-laws with exponents as labelled. The vertical dashed line represents the minimal angular separation resolved by our double-difference method.

In summary, we evidenced that (1) rupture events are mostly organized in multiplets, which result from the occurrence of weakly clustered series of multiplets, that individually corresponds to a set of homogeneously distributed ruptures, (2) only the largest ruptures ($M_w > -5.5$) have the potential to trigger other ruptures, mostly within a few tenths of second. The lack of triggering at small magnitudes ($M_w < 5.5$, which correspond to 99.9 % of the ruptures) along with the homogeneously distributed occurrence times within multiplets argue for a mostly passive role of the detected s during the deformation.

3.3.2. Spatial Clustering of the Ruptures

The spatial correlations between events with respect to their locations has been investigated by computing the same correlation integral as in Equation (8), but in space. We consider all pairs of ruptures separated by an angular separation less than $\Delta\alpha$, with $\Delta\alpha = \alpha_i - \alpha_j$, cf. Figure 12. The slip along the fault eventually impacts the spatial distribution of the ruptures, as asperities can move relative to the fixed plate. This explains why the correlation integral exhibits a simple $C(\Delta\alpha) \propto \Delta\alpha$ regime, indicative of a uniform density of asperities along the fault over long time scales (about two full revolutions are accomplished during this 5 hour long experiment).

Limiting the correlation integral to pairs separated in time by at maximum 12 s, 120 s or 480 s (corresponding to imposed rotation angles of 0.5°, 5°, and 20°) a power law regime is observed for angular intervals above 0.3° . This lower cut-off is related to the resolution of our estimated angular positions obtained by the double difference method. Above this cut-off, we observe different regimes according to the time separation limits imposed. For short time scales (up to 12 s), the correlation dimension δ is 0.1. At this time scale, which is similar to the average multiplet duration, we observe very few pairs of ruptures belonging to distinct multiplets. For longer time scales, the correlation dimension increases to $\delta = 0.6$ for a maximum separation of 420 s (corresponding to a rotation of 20°). This regime is for angle separations between 0.3° and 14° (= 53 mm), and corresponds to pairs with ruptures belonging to different multiplets. This power-law regime is thus the signature of the spatial clustering of multiplets, hence of resisting asperities, up to a distance of a few centimeters.

3.4. Relation Between Torque Drops and Rupture Magnitude

We showed in Section 3.1 that the detected seismicity and torque are not correlated, when counting all the ruptures. We now investigate how this relationship depends on the size of the rupture. To do so, several magnitude groups are defined and the averaged torque variation within a ± 2 s time intervals centered on the rupture occurrence time, see Figure 13. This method is inspired by the work of Frank et al. (2015). For the smallest magnitudes that represent $M_w \leq -6.0$, about 98% of the ruptures, a smooth torque release is observed over several seconds with no sharp torque drop. For ruptures in the magnitude ranges $M_w \in [-6.0, -5.5]$ and $M_w \in [-5.5, -5.0]$, the torque is released more suddenly (within a few 1/10th of a second) by $\Delta\Gamma = 0.32$N.m and $\Delta\Gamma = 1.19$N.m, respectively. Estimating average torque changes are below or close to

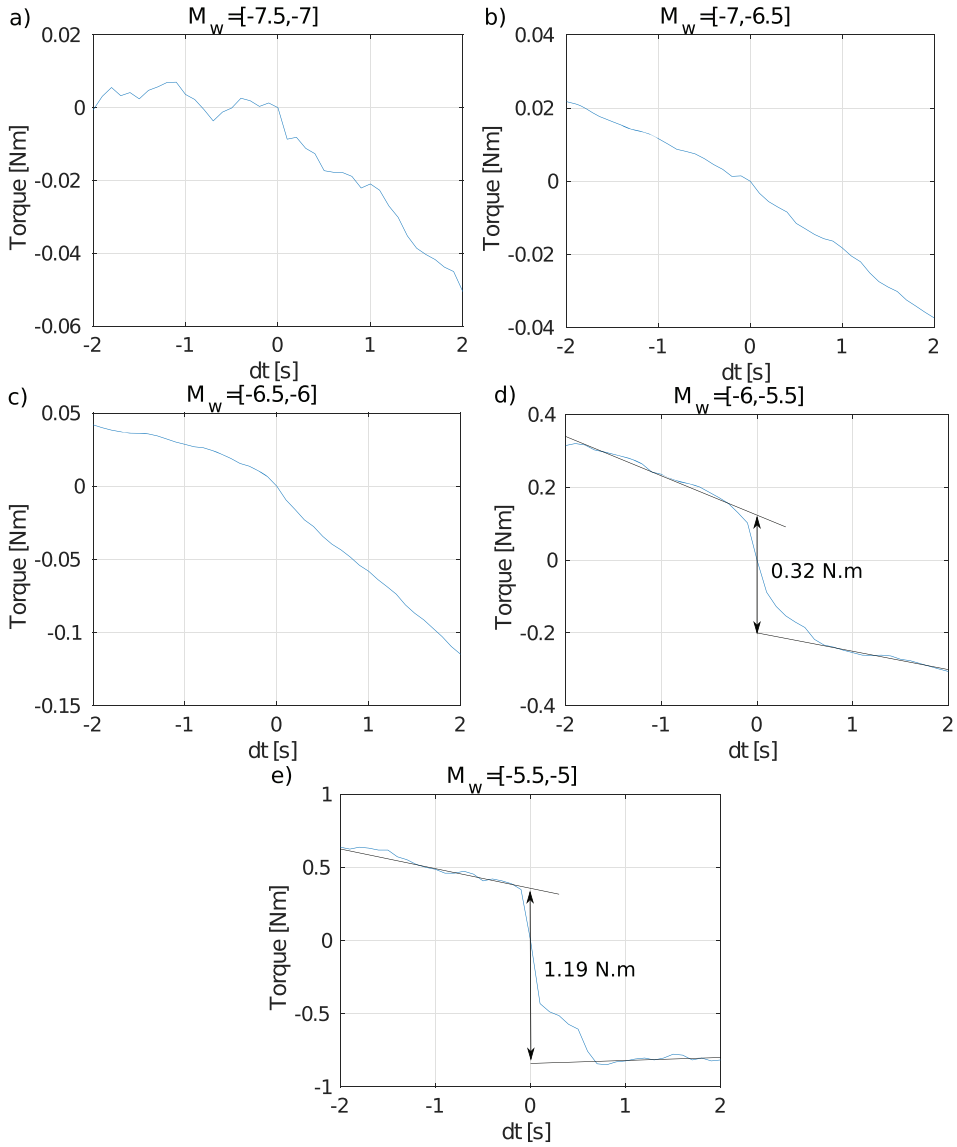

Figure 13. Average torque change observed in a ± 1 s-long interval related to each main rupture sorted according to its magnitude. Solid lines are the best linear fits before and after the sudden torque drops.

the accuracy of the torquemeter. However, by stacking the torque variation allows to go below this limits, the accuracy increasing with the number of observations stacked.

Rather than selecting ruptures according to their sizes and perform a stack of the torque, a simple linear model is design to fit the time variation of the torque increments, $\delta\Gamma_t$ (computed for a 0.1 s-long time step), using the rupture magnitudes. In the model, at any given time step, the modelled torque increment, $\widehat{\delta\Gamma}_t$, is the sum of a strengthening parameter S_0, and magnitude-related torque drops, Δc_m, caused by the ruptures occurring in the same time step (of 0.1 s duration):

$$\widehat{\delta\Gamma}_t = S_0 - \sum_m \Delta c_m n_{m,t} \tag{9}$$

where $n_{m,t}$ is the number of ruptures in this time step t, and in the magnitude interval of index m. The torque drop related to each magnitude interval, Δc_m, is computed by minimizing the quadratic cost function $J = \sum_t (\widehat{\delta\Gamma}_t - \delta\Gamma_t)^2$. Minimizing J leads to the solution $\underline{C} = \underline{\underline{A}}^{-1}\underline{\Delta C}$, with $\underline{C}={}^t(S_0, \Delta c_1, \Delta c_2, \dots)$ the column-vector that contains the strengthening parameter and torque drops associated with each magnitude

bin, $\underline{\Delta C}={}^t(\sum_t \delta\Gamma_t, \sum_t n_{1,t}\delta\Gamma_t, \sum_t n_{2,t}\delta\Gamma_t \dots)$ the column-vector containing the torque increment information, and $\underline{\underline{A}}$ defined as:

$$\underline{\underline{A}} = \begin{pmatrix} T & -N_1 & -N_2 & \dots \\ N_1 & -M_{11} & -M_{12} & \dots \\ N_2 & -M_{21} & -M_{22} & \dots \end{pmatrix} \tag{10}$$

with T the number of time steps, N_m the number of ruptures within each magnitude interval, and $M_{ij} = \sum_t n_{i,t}n_{j,t}$. Based on Figure 13, we define three magnitude bins: $m_1 \in [-8,-6]$, $m_2 \in [-6,-5.5]$ and $m_3 \in [-5.5,-5]$. We obtain a strengthening rate $S_0 = 7.0\times10^{-3} N.m.s^{-1}$, and torque drops per time step (0.1 s) $\Delta c_1 = 3.0\times10^{-3}$N.m, $\Delta c_2 = 7.5\times10^{-2}$N.m and $\Delta c_3 = 3.2\times10^{-1}$N.m. The total torque drops related to each magnitude class are $N_1\Delta c_1 = 66$N.m, $N_2\Delta c_2 = 25$N.m and $N_3\Delta c_3 = 12$N.m. All the magnitude intervals thus significantly contribute to the total torque drops.

The torque drop associated to a rupture of length L and slip U is:

$$\Delta\Gamma = r\frac{\mu U}{L}LW\frac{L}{2\pi r} = \frac{1}{2\pi}\mu ULW = \frac{M_0}{2\pi} \tag{11}$$

hence, $\Delta\Gamma$ is directly proportional to M_0. The relatively large number of small ruptures then compensates for the decay of seismic moment (or torque drop), resulting in this apparent stationarity of $N_i\Delta c_i$ with magnitude. This states that the number of earthquakes (in 10^{-bM_w}) compensates the rapid decay of the seismic moment (in $10^{1.5M_w}$) at small magnitude. As a consequence, convergence of the moment (or torque) release rate cannot be reached, as one would need to know all the ruptures down to an a priori unknown cut-off magnitude to allow for a meaningful estimate. In Section 4.2.2 a method to infer this unknown lower magnitude cut-off is developed.

3.5. Slip Budget: Seismic Coupling Coefficient

One of the aim of this study is to characterize the slip budg et along the fault, i.e., the proportion of seismic slip compared with the imposed one. The seismic coupling coefficient χ is defined as the ratio between the cumulative seismic slip U_s and the imposed slip. Seismic slip is $U_s = \frac{1}{\mu 2\pi r W}\sum_i M_{0,i}$, where $2\pi r$ is the fault length, and W the fault width (Brune, 1968). Assuming a constant ice thickness of 6 mm, the total slip released by the ruptures is $U_s = 2.1\times10^{-4}$m at the end of the experiment. The total imposed slip is $U_{tot} = 2.88$m (i.e., 5 hours at 10 r.p.d.), yielding $\chi = 7\times10^{-5}$. Please note that this is an underestimation: the contribution from small undetected seismic ruptures, below the detection level of the monitoring system (i.e., not detected with a detection probability of one, or too small to be correctly characterized), is expected to be significant, as already commented.

4. Discussion

4.1. Large B-Value: what Prevent Ruptures to Grow Big?

The rupture size distribution of the earthquakes is well described by the Gutenberg-Richter law's that writes (Gutenberg & Richter, 1954): $log_{10}N = a - bM_w$. The b-value is the slope of the power-law decrease that relates the earthquake size and the frequency. A b-value close to one is generally found, yet significant departures from this value have been observed in the crust and in laboratory experiments (Utsu, 2002). Especially, the b-value increases with decreasing normal stress (Scholz, 1968a; 2002; Schorlemmer et al., 2005; Wiemer & Wyss, 2002).

Scholz (2015) argues for a linear relationship between b and deviatoric stress. In some geophysical contexts, large values up to $b \simeq 2$ are found, for example in the context of volcanic systems (Gerstenberger et al., 2001; Mori & Abercrombie, 1997; Wiemer et al., 1998; Wiemer & Katsumata, 1999; Wiemer & Wyss, 2002) and along mid-oceanic transform faults (Kanamori & Anderson, 1975; Scholz, 2002; Roland & McGuire, 2009). A b-value as large as 2.5 has been observed for non-volcanic tremor along the Parkfield section of the San Andreas fault (Staudenmaier et al., 2019).

The rupture size distribution of laboratory micro-seismic or acoustic emission events obey a frequency-magnitude distribution similar to crustal seismicity (Scholz, 1968b; 1968c). In our study, for a

rotation rate of 10 rpd, we observe a Gutenberg-Richter distribution with a b-value of 3.0 based on 12195 ruptures with a magnitude M_w >-6.4, implying that ruptures hardly propagate over long distances. Some explanations are proposed hereinafter: (1) at low normal stress (since no normal stress is applied across the fault), strength is supported by scattered, isolated asperities that more seldomly break collectively (Bowden & Tabor, 1939; Logan & Teufel, 1986; Roux et al., 1993; Scholz, 1968a). These asperities result from roughness profile mismatch between the two sides of the fault. Even the largest asperity is likely far away from its neighbours, so that a rupture can hardly propagate over a long distance and is likely restricted to the breaking asperity; (2) the low normal stress prevents the accumulation of large shear stresses, hence limits the rupture propagation as the amount of elastic energy stored is small. This can explain the negative correlation between the *b*-value and normal stress observed by Rivière et al. (2018) in friction laboratory experiments; (3) if the normal stress falls below a critical value (related to the fault equivalent stiffness), the deformation regime is conditionally stable except on localized patches where the stress concentrates (Scholz, 1998).

4.2. Seismic Coupling

The seismic coupling estimated from the detected ruptures is $\chi = 7 \times 10^{-5}$ (see Section 3.5). This value is likely under-estimated and too-small-to-be-detected brittle ruptures likely control the deformation. In that case, the fault deforms in what can be called an apparent aseismic regime for which ruptures do occur (potentially up to $\chi = 1$). Most of them being too small to be detected. In the following sections we develop on (1) why a value of b larger than 1.5 implies that small ruptures are efficient to release seismic slip; (2) what is the minimum rupture size that can be expected, as a function of the seismic coupling.

4.2.1. Deformation Governed by Small Undetected Ruptures?

Given the scaling relationship between seismic moment and moment magnitude $M_0 \propto 10^{1.5M_w}$ (Kanamori & Anderson, 1975) and between the number of events and the magnitude, $N(M_w) \propto 10^{-bM_w}$ (Gutenberg & Richter, 1954), the total seismic moment is proportional to:

$$\int_{M_w^{min}}^{M_w^{max}} dm \quad 10^{(1.5-b)M_w}, \tag{12}$$

hence to $10^{k(M_w^{max}-M_w^{min})}$, where $k = 1.5 - b$. In the case where $b < 1.5$, i.e., $k > 0$, this integral is dominated by the upper cut-off, in $10^{kM_w^{max}}$. Knowing M_w^{max} then allows for a proper estimation of the total seismic moment, and hence of the seismic coupling (Scholz & Campos, 2012). Conversely, for $b > 1.5$, the dominant term is $10^{kM_w^{min}}$, and computation of the total seismic moment requires knowing M_w^{min}. Undetected small ruptures do contribute to the total slip, and cannot be dismissed from the slip budget. These undetected ruptures refer to brittle, seismic, ruptures that are too small to be detected by the monitoring system used in this study. Hence, the possibility that most of the slip along the fault is accommodated by brittle ruptures, but at very small scale, cannot be rejected. This situation would correspond to an apparent aseismic motion, instead of an effective aseismic motion implying plasticity and/or stable sliding. This could also explain the relatively low correlation between the detected rupture rate and the torque time series: partial release of the fault shear strength, evidenced by a decrease in torque, could be fully accommodated by cracking made of ruptures too small to be detected. This is in strong contrast with what is typically observed in seismology, where 90% of the tectonic slip is accommodated by the largest earthquakes, of magnitude greater than $M_w^{max} - 2$ (Marsan, 2005), so that only the biggest earthquakes are needed to estimate the long-term moment release rate (Brune, 1968; Scholz, 1972; Scholz & Cowie, 1990; Shen et al., 1994). This regime was also recently described by Staudenmaier et al. (2019) to characterize the distribution of energy release through slip during non-volcanic tremor (NVT) along the San Andreas fault in Parkfield. Similarly to us, they conclude that the observed $b > 1.5$ distribution correspond to a 'invisible-seismic' regime (in their own terms). NVT occurs at greater depths than 'normal' seismicity, so that a $b > 1.5$ distribution is likely due to isolated asperities that cannot easily propagate large ruptures. Also, we here follow a different method for inferring the possible minimum size of rupture. Instead of using the material grain size as the lower limits of seismic slip to infer the minimal rupture magnitude, with our method the seismic coupling is kept as a control parameter, since, as explained below, it cannot be deduced unambiguously from our observations.

4.2.2. Could One Estimate a Coupling Coefficient?

We showed (section 4.2) that the coupling coefficient cannot be estimated accurately with the present acquisition setup. What would be the minimal rupture size to obtain a physically relevant value?

Ruptures are detected down to a moment magnitude $M_w = -7.9$, but clear departure from the Gutenberg-Richter law occurs at $M_w < -6.4$. Our detection algorithm is thus parameterized in a way that ruptures with magnitude $M_w < -6.4$ are not detected with certainty. The extent to which the true Gutenberg-Richter law remains valid below this magnitude is unknown, at least given our detection method.

However, since we estimate the $b-$value to be significantly greater than 1.5, we now demonstrate that the lower physical cut-off of the Gutenberg-Richter law can be inferred from simple arguments, that are similar to those evoked in crustal seismo-tectonics to evaluate the upper limit (or maximum magnitude) of the Gutenberg-Richter law (e.g., Avouac, 2015 for a review). The fault accumulates seismic moment according to the rate:

$$\dot{M}_{0,\Sigma} = \mu v \chi 2\pi r H \tag{13}$$

with v the imposed velocity ($v = 1.6\times10^{-4}$m.s^{-1}), μ the ice stiffness ($\mu = 3.52\times10^{9}$Pa), $2\pi rH = 8.3\times10^{-3}$m^2, and χ the coupling coefficient, which is largely unknown ($7\times10^{-5} < \chi < 1$, see discussion in section 4.2). This accumulated moment is released according to a Gutenberg-Richter law with probability density in $f(M_w) \propto e^{-\beta M_w}$ ($\beta = b\ln 10$) for $M_w^{min} \leq M_w \leq M_w^{max}$, and a rate $\dot{N}_0$ known at magnitude $M_w \geq M_w^0$. Here, we find that $M_w^{max} = -5.5$, and the rate is $\dot{N}_0 = 0.28$ s^{-1} for $M_w \geq -6.4$ ruptures (we used -6.4 as M_w^0 as the detection is complete above this magnitude). The goal is to estimate M_w^{min}.

The average seismic moment released by a rupture of random magnitude as distributed according to the density $f(M_w) = \frac{\beta e^{-\beta M_w}}{e^{-\beta M_w^{min}} - e^{-\beta M_w^{max}}}$ is

$$\overline{M}_0 = \int_{M_w^{min}}^{M_w^{max}} dm f(M_w) M_0(M_w) = \frac{\beta}{\beta - \gamma} M_{0,min} \tag{14}$$

where we used the fact that $M_0(m) \propto e^{\gamma M_w}$ with $\gamma = 1.5\ln 10$, and assumed that $\beta > \gamma$ since $b > 1.5$.

The rate of release is thus $\dot{M}_{0,\Sigma} = \dot{N}_0 e^{-\beta(M_w^{min} - M_w^0)}\overline{M}_0$ where the term $\dot{N}_0 e^{-\beta(M_w^{min} - M_w^0)}$ is the rupture rate extrapolated down to magnitude M_w^{min}. This can be rewritten as

$$\dot{M}_{0,\Sigma} = \frac{\dot{N}_0 \beta}{\beta - \gamma} M_0 e^{(\beta-\gamma)(M_w^0 - M_w^{min})} \tag{15}$$

where M_0 is here the seismic moment at magnitude M_w^0. Over long time scales, the accumulation and release of seismic moment must be equal to one another, imposing that

$$\mu v \chi 2\pi r H = \frac{\dot{N}_0 \beta}{\beta - \gamma} M_0 e^{(\beta-\gamma)(M_w^0 - M_w^{min})}. \tag{16}$$

Only χ and M_w^{min} are unknown here. We can thus infer M_w^{min} for a specific (guessed) value of χ. The two limit cases are (1) $\chi = 7\times10^{-5}$, which yield $M_w^{min} = -6.6$ and (2) $\chi = 1$, giving $M_w^{min} = -9.2$. We detect ruptures down to a magnitude -8, but the detection is complete only for $M_w > -6.4$. Our simplified model assumes a sharp cut-off of the Gutenberg-Richter law at M_w^{min}. Smoother cut-offs of the Gutenberg-Richter law would result in lower $\overline{M}_0$ values, hence lower M_w^{min}. It is therefore difficult to effectively determine M_w^{min} based on Figure 7 alone: the lack of resolution below the magnitude of completeness -6.4 does not allow to probe M_w^{min}. In any case, the interval $-9.2 < M_w^{min} < -6.6$ can be considered as a weak constraint on the minimum (physical) cut-off magnitude of the power-law distribution. We can moreover anticipate that a change in the Gutenberg-Richter law is likely to occur for $L < W$, i.e., a change in b-value at small magnitudes, which we have not accounted for by lack of constraints.

4.3. Clustering in Multiplets

A time and space clustering of ruptures is observed during the experiment. The characteristics of the clustering reflect that the interaction between multiplets. About 71 %, of the ruptures belong to multiplets, i.e., finite, short duration (of the order of several seconds, cf. Section 3.3) swarms of ruptures made of events with a characteristic size (cf. Figure 8). These multiplets are classically associated with small asperities embedded in an otherwise stable sliding slip interface (Chen & Lapusta, 2009; Delahaye et al., 2009; Lengliné & Marsan, 2009; Nadeau & McEvilly, 1999; Uchida et al., 2003; Segall et al., 2006) and thus can be considered as a marker of stable sliding.

Our observation of the predominance of short-duration multiplet clusters therefore points to the possibility that some of the slip is accommodated by episodic aseismic slip driving the multiplet asperities. We suspect that our torque measurements cannot resolve these episodes, as they integrate deformation over the whole fault, while the short-sized multiplets suggest that these slip episodes are localized.

4.4. Comparison with Crustal Systems

In our study, the imposed shear sliding along the fault leads to an abundant swarm-like seismic activity. The experimental conditions are in some ways similar to certain geophysical settings: i) the difference in stiffness between the two fault compartments, which could promote stable sliding, share similarities with the transition zone in the crust; ii) as no normal stress is imposed across the fault, it can be seen as equivalent to a reduced normal stress resulting from a high pore-pressure. We propose that, instead of being only a by-product of a potential aseismic slip, the multiplets and the small seismic ruptures could potentially account for a large part of the imposed slip. In such case, the fault is likely locked and aseismic slip results in the loading of the asperities. Then, fault slip occurs through the successive shear failures of small locked asperities. The short durations of our multiplets bear some similarities with the observation that low-frequency earthquakes occur in short bursts, highlighting that 'stable' aseismic sliding could indeed be intermittent (Lengliné et al., 2017).

The frequency-size distribution of the ruptures, with a *b*-value larger than 1.5, implies that the small seismic moment released individually by the ruptures is compensated by the large number of ruptures. The slip partitioning between unstable and stable slip in such a deformation regime, characterized by the seismic coupling, remains an unresolved question. In addition to detection problems, since ruptures of all magnitudes contribute significantly to the deformation, a robust estimation of the seismic coupling requires the detection of all the ruptures. This condition is out of the detection range of any existing seismic array, even in laboratory. In this study, we have shown that magnitudes down to -9.2 need to be detected for us to estimate the seismic coupling. Similarly, Staudenmaier et al. (2019) found that events with a moment magnitude of -7 could accommodate the entire fault deformation observed in the Parkfield section of the San Andreas Fault.

Thus, the deformation regime observed in our experimental setting shares several similarities (swarm-like activity, apparent low coupling, high *b*-value potentially greater than 1.5), with crustal systems, which are all characterized by a relatively high temperature: (1) volcanic systems; (2) oceanic transform faults, known to be characterized by large *b*-values and low dispersion in earthquake magnitudes (Sykes, 1970). The associated seismicity is characterized by a swarm-like behaviour (Boettcher & Jordan, 2001; McGuire, 2003; McGuire et al., 2005; Roland & McGuire, 2009), and obviously by strike-slip mechanism in a thin crust with a high thermal gradient, low normal stress, and low seismic coupling Cowie et al. (1993); Bird et al. (2002), as with our laboratory fault; (3) the transition zone of plate boundary faults, between a locked layer at shallow depth and a freely sliding interface at greater depths. This transition zone is known to potentially host episodic slow slip and non-volcanic tremor, the latter phenomenon being related to small, isolated asperities repeatedly failing in bursts of low frequency earthquakes (Lengliné et al., 2017; Obara, 2002; Thomas et al., 2018; Shelly et al., 2006; Staudenmaier et al., 2019). There, brittle failure is usually considered to account for only a small portion of the deformation. Recently, Staudenmaier et al. (2019) has proposed that undetected earthquakes could make up for the missing seismic moment. Based on our observations, we suggest that the same mechanism occurs along our experimental fault, although we cannot dismiss the possibility that aseismic slip in the true sense also occurs.

Finally, the time distribution of the ruptures belonging to a multiplet suggests that the events obey a Poisson process. A Poisson distribution of recurrences times between ruptures is expected for declustered catalogs (Kagan & Jackson, 1991) and during seismic swarms (De Natale & Zollo, 1986; Peng & Gomberg, 2010). As a large number of tremors have been detected on the San Andreas Fault (Shelly, 2017), performing an analysis of the time distribution of the events can be pertinent.

In consequence, both in the laboratory and in nature, *b*-values larger than 1.5, or even more, are associated with an “apparent” aseismic regime for which transient slip, promoted by low normal stress, and caused by the failure of multiple small locked patches that are sufficiently far away from each other to prevent fracture propagation over large distance. In that case, tremors are not only by-product of slow slip but might be accommodating seismically an important part of the deformation.

If so, in regions of the world where NVT are detected, e.g., Japan, Cascadia, New Zealand, San Andreas (Kao et al., 2010; Nadeau & Dolenc, 2005; Nadeau & Guilhem, 2009; Obara, 2002; Obara et al., 2004; Rogers & Dragert, 2003; Shelly, 2017; Shelly et al., 2006, 2007; Wech & Creager, 2007), and which have been considered as deforming aseismically, a significant fraction of slip is potentially accommodated by undetected seismic ruptures. Therefore, the estimation of the seismic coupling at depth is difficult since most of the energy is inaccessible to current seismic arrays.

5. Conclusion

During this experiment, we explore the behaviour of a quasi-stationary fault that accommodates the imposed slip by brittle deformation. We observe very little correlation between the seismicity rate and torque fluctuations, although limiting our attention to the largest ruptures effectively leads to a clear connection between torque drop amplitude and rupture magnitude. This relation is further evidenced by a model that links torque increments to rupture occurrence times over the whole experiment. The relatively weak relationship between ruptures and torque readily suggest that deformation is either mostly aseismic, or that it is brittle but the corresponding cracking goes mostly undetected by the monitoring system.

The largest magnitudes are distributed according to a Gutenberg-Richter law with a b-value of 3.0. This large value, being remarkably greater than the critical 1.5 value, implies that contrary to what is observed for crustal earthquakes, at the explored sliding rate and temperature, the deformation can be controlled by the smallest (non-detectable) ruptures, down to a minimum magnitude in the range $-9.2(\text{if}\chi = 1) < M_w < -6.6$ (if $\chi = 7 \times 10^{-5}$, which is the observed coupling value). The fault thus potentially accommodates all the imposed deformation through fracturing, but in an apparent aseismic regime for which the bulk of the brittle process is not directly measurable by our acquisition set-up. Multiplets contain about 70 % of the detected activity, and correspond to slip episodes lasting about 10 s (on average) during which a resisting asperity fails repeatedly. Very little triggering (i.e., ruptures causally triggering the occurrence of subsequent ruptures) is observed during these episodes, the micro-ruptures being passive by-products of the aseismic slip. This deformation regime is remarkably different from what is observed for seismogenic crustal faults, but bears strong similarities with episodic slow slip and non-volcanic tremor observed at the transition depths between locked and freely slipping plate boundary faults. The fault deformation is likely the results of the sum of three slip regimes: aseismic (enhanced by the low nomal stress), seismic (on locked asperities) and an 'apparent' aseismic. Therefore, regions of the world for which important tremors activities have been detected might partially move, not through aseismic creep, but through undetected stick-slip events that in some case are more efficient to accommodate fault deformation. A detailed analysis of the seismicity, specific *b*-values, clustering in time and space might help to identified the regions for which an “apparent” aseismic slip is the norm.

Acknowledgments
This work was supported by a grant from the Université Savoie Mont-Blanc, by INP-Grenoble and the Université Grenoble Alpes in the framework of “Grenoble Innovation Recherche AGIR”. It benefited from the financial support from the French “Agence Nationale de la Recherche” (project AtypicSSE). We also would like to thank the reviewers, who made constructive comments. The datasets are available on GitHub: https://github.com/lachaudc/Micro-seismic-monitoring-of-a-floating-ice-plate

References

Aki, K. (1966). Generation and propagation of g waves from the niigata earthquake of june 16, 1964. Part 2. Estimation of earthquake movement, released energy, and stress-strain drop from the g wave spectrum. *Bulletin of the Earthquake Research Institute*, *44*, 73–88.

Allen, R. (1982). Automatic phase pickers: Their present use and future prospects. *Bulletin of the Seismological Society of America*, *72*(6B), S225–S242.

Avouac, J.-P. (2015). From Geodetic Imaging of Seismic and Aseismic Fault Slip to Dynamic Modeling of the Seismic Cycle. *Annual Review of Earth and Planetary Sciences*, *43*, 233–271. https://doi.org/10.1146/annurev-earth-060614-105302

Barnes, P., & Tabor, D. (1966). Plastic Flow and Pressure Melting in the Deformation of Ice I. *Nature*, *210*, 878–882. https://doi.org/10.1038/210878a0

Barnes, P., Tabor, D., & Walker, J. C. F. (1971). The Friction and Creep of Polycrystalline Ice. *Proceedings of the Royal Society of London Series A*, *324*, 127–155. https://doi.org/10.1098/rspa.1971.0132

Batto, R., & Schulson, E. (1993). On the ductile-to-brittle transition in ice under compression. *Acta metallurgica et materialia*, *41*(7), 2219–2225.

Beyreuther, M., Barsch, R., Krischer, L., Megies, T., Behr, Y., & Wassermann, J. (2010). Obspy: A python toolbox for seismology. *Seismological Research Letters*, *81*(3), 530–533.

Bird, P., Kagan, Y. Y., & Jackson, D. D. (2002). Plate tectonics and earthquake potential of spreading ridges and oceanic transform faults. *Plate Boundary Zones*, *30*, 203–218.

Boettcher, M., & Jordan, T. (2001). Seismic behavior of oceanic transform faults. *AGU Fall Meeting Abstracts*.

Bohnhoff, M., Dresen, G., Ellsworth, W. L., & Ito, H. (2009). Passive seismic monitoring of natural and induced earthquakes: Case studies, future directions and socio-economic relevance, *New Frontiers in Integrated Solid Earth Sciences* (pp. 261–285). Dordrecht: Springer.

Bowden, F. P., & Tabor, D. (1939). The Area of Contact between Stationary and between Moving Surfaces. *Proceedings of the Royal Society of London Series A*, *169*, 391–413. https://doi.org/10.1098/rspa.1939.0005

Brune, J. N. (1968). Seismic moment, seismicity, and rate of slip along major fault zones. *Journal of Geophysical Research*, *73*(2), 777–784.
Candela, T., & Brodsky, E. E. (2015). The minimum scale of grooving on faults. *AGU Fall Meeting Abstracts*, T43C–3009.
Caswell, T. E., Cooper, R. F., & Goldsby, D. L. (2015). The constant-hardness creep compliance of polycrystalline ice. *Geophysical Research Letters*, *42*, 6261–6268. https://doi.org/10.1002/2015GL064666
Chen, T., & Lapusta, N. (2009). Scaling of small repeating earthquakes explained by interaction of seismic and aseismic slip in a rate and state fault model. *Journal of Geophysical Research*, *114*, B01311. https://doi.org/10.1029/2008JB005749
Cowie, P. A., Scholz, C. H., Edwards, M., & Malinverno, A. (1993). Fault strain and seismic coupling on mid-ocean ridges. *Journal of Geophysical Research*, *98*, 17.
De Natale, G., & Zollo, A. (1986). Bulletin of the Seismological Society of America, *76*(3), 801–814.
Delahaye, E. J., Townend, J., Reyners, M. E., & Rogers, G. (2009). Microseismicity but no tremor accompanying slow slip in the Hikurangi subduction zone, New Zealand. *Earth and Planetary Science Letters*, *277*, 21–28. https://doi.org/10.1016/j.epsl.2008.09.038
Dieterich, J. H. (1972). Time-dependent friction in rocks. *Journal of Geophysical Research*, *77*, 3690–3697. https://doi.org/10.1029/JB077i020p03690
Dieterich, J. H. (1978). Time-dependent friction and the mechanics of stick-slip. *pure and applied geophysics*, *116*(4-5), 790–806.
Dieterich, J. H. (1979a). Modeling of rock friction: 1. Experimental results and constitutive equations. *Journal of Geophysical Research*, *84*, 2161–2168. https://doi.org/10.1029/JB084iB05p02161
Dieterich, J. H. (1979b). Modeling of rock friction: 2. Simulation of preseismic slip. *Journal of Geophysical Research*, *84*, 2169–2175. https://doi.org/10.1029/JB084iB05p02169
Duval, P., Ashby, M., & Anderman, I. (1983). Rate-controlling processes in the creep of polycrystalline ice. *The Journal of Physical Chemistry*, *87*(21), 4066–4074.
Fortt, A., & Schulson, E. (2007). The resistance to sliding along coulombic shear faults in ice. *Acta materialia*, *55*(7), 2253–2264.
Frank, W. B., Radiguet, M., Rousset, B., Shapiro, N. M., Husker, A. L., Kostoglodov, V., et al. (2015). Uncovering the geodetic signature of silent slip through repeating earthquakes. *Geophysical Research Letters*, *42*, 2774–2779. https://doi.org/10.1002/2015GL063685
Gerstenberger, M., Wiemer, S., & Giardini, D. (2001). A systematic test of the hypothesis that the b value varies with depth in california. *Geophysical Research Letters*, *28*, 57–60.
Glen, J. W. (1955). The Creep of Polycrystalline Ice. *Proceedings of the Royal Society of London Series A*, *228*, 519–538. https://doi.org/10.1098/rspa.1955.0066
Goebel, T. H. W., Schorlemmer, D., Becker, T. W., Dresen, G., & Sammis, C. G. (2013). Acoustic emissions document stress changes over many seismic cycles in stick-slip experiments. *Geophysical Research Letters*, *40*, 2049–2054. https://doi.org/10.1002/grl.50507
Goldsby, D. L., & Kohlstedt, D. L. (2001). Superplastic deformation of ice: Experimental observations. *Journal of Geophysical Research*, *106*, 11,017–11,030. https://doi.org/10.1029/2000JB900336
Gomberg, J., Agnew, D. C., & Schwartz, S. Y. (2016). Alternative source models of very low frequency events. *Journal of Geophysical Research: Solid Earth*, *121*, 6722–6740. https://doi.org/10.1002/2016JB013001
Goodfellow, S. D., & Young, R. P. (2014). A laboratory acoustic emission experiment under in situ conditions. *Geophysical Research Letters*, *41*, 3422–3430. https://doi.org/10.1002/2014GL059965
Got, J.-L., Fréchet, J., & Klein, F. W. (1994). Deep fault plane geometry inferred from multiplet relative relocation beneath the south flank of kilauea. *Journal of Geophysical Research*, *99*(B8), 15,375–15,386.
Grassberger, P., & Procaccia, I. (1983). Characterization of strange attractors. *Physical Review Letters*, *50*, 346–349.
Gutenberg, B., & Richter, C. (1954). *Seismicity of the earth*. Princeton, NJ: Princeton University Press.
Hartley, R., & Behringer, R. (2003). Logarithmic rate dependence of force networks in sheared granular materials. *Nature*, *421*(6926), 928–931.
Heaton, T. H. (1990). Evidence for and implications of self-healing pulses of slip in earthquake rupture. *Physics of the Earth and Planetary Interiors*, *64*, 1–20. https://doi.org/10.1016/0031-9201(90)90002-F
Kagan, Y. Y., & Jackson, D. D. (1991). Long-Term Earthquake Clustering. *Geophysical Journal International*, *104*, 117–134. https://doi.org/10.1111/j.1365-246X.1991.tb02498.x
Kanamori, H., & Anderson, D. L. (1975). Theoretical basis of some empirical relations in seismology. *Bulletin of the Seismological Society of America*, *65*(5), 1073–1095.
Kao, H., Wang, K., Dragert, H., Kao, J. Y., & Rogers, G. (2010). Estimating seismic moment magnitude (M_w) of tremor bursts in northern Cascadia: Implications for the "seismic efficiency" of episodic tremor and slip. *Geophysical Research Letters*, *37*, L19306. https://doi.org/10.1029/2010GL044927
Kwiatek, G., Goebel, T. H. W., & Dresen, G. (2014). Seismic moment tensor and b value variations over successive seismic cycles in laboratory stick-slip experiments. *Geophysical Research Letters*, *41*, 5838–5846. https://doi.org/10.1002/2014GL060159
Lamb, H. (1917). On Waves in an Elastic Plate. *Proceedings of the Royal Society of London Series A*, *93*, 114–128. https://doi.org/10.1098/rspa.1917.0008
Lengliné, O., Frank, W., Marsan, D., & Ampuero, J. P. (2017). Imbricated slip rate processes during slow slip transients imaged by low-frequency earthquakes, *AGU Fall Meeting Abstracts* (Vol. 2017, pp. S53F–05).
Lengliné, O., & Marsan, D. (2009). Inferring the coseismic and postseismic stress changes caused by the 2004 $M_w = 6$ parkfield earthquake from variations of recurrence times of microearthquakes. *Journal of Geophysical Research*, *114*, B10303. https://doi.org/10.1029/2008JB006118
Lherminier, S., Planet, R., Vehel, V. L. D., Simon, G., Vanel, L., Måløy, K. J., & Ramos, O. (2019). Continuously Sheared Granular Matter Reproduces in Detail Seismicity Laws. *Physical Review Letters*, *122*(21), 218501. https://doi.org/10.1103/PhysRevLett.122.218501
Logan, J. M., & Teufel, L. W. (1986). The effect of normal stress on the real area of contact during frictional sliding in rocks. *Pure and Applied Geophysics*, *124*, 471–485. https://doi.org/10.1007/BF00877212
Madariaga, R. (1976). Dynamics of an expanding circular fault. *Bulletin of the Seismological Society of America*, *66*(3), 639–666.
Marone, C. (1998). Laboratory-Derived Friction Laws and Their Application to Seismic Faulting. *Annual Review of Earth and Planetary Sciences*, *26*, 643–696. https://doi.org/10.1146/annurev.earth.26.1.643
Marsan, D. (2005). The role of small earthquakes in redistributing crustal elastic stress. *Geophysical Journal International*, *163*, 141–151.
McGuire, J. (2003). Immediate foreshock sequences of oceanic transform earthquakes on the east pacific rise. *The Bulletin of the Seismological Society of America*, *93*, 948–952.
McGuire, J. J., Boettcher, M. S., & Jordan, T. H. (2005). Foreshock sequences and short-term earthquake predictability on east pacific rise transform faults. *Nature*, *434*, 457–461.
McLaskey, G. C., Kilgore, B. D., Lockner, D. A., & Beeler, N. M. (2014). Laboratory Generated M -6 Earthquakes. *Pure and Applied Geophysics*, *171*, 2601–2615. https://doi.org/10.1007/s00024-013-0772-9

McLaskey, G. C., Lockner, D. A., Kilgore, B. D., & Beeler, N. M. (2015). A Robust Calibration Technique for Acoustic Emission Systems Based on Momentum Transfer from a Ball Drop. *The Bulletin of the Seismological Society of America*, *105*, 257–271. https://doi.org/10.1785/0120140170

Mclaskey, G. C., & Yamashita, F. (2017). Slow and fast ruptures on a laboratory fault controlled by loading characteristics. *Journal of Geophysical Research: Solid Earth*, *122*, 3719–3738. https://doi.org/10.1002/2016JB013681

Miller, B., O'Hern, C., & Behringer, R. (1996). Stress fluctuations for continuously sheared granular materials. *Physical Review Letters*, *77*(15), 3110–3113.

Moreau, L., Lachaud, C., Théry, R., Predoi, M. V., Marsan, D., Larose, E., et al. (2017). Monitoring ice thickness and elastic properties from the measurement of leaky guided waves: A laboratory experiment. *The Journal of the Acoustical Society of America*, *142*(5), 2873–2880.

Mori, J., & Abercrombie, R. E. (1997). Depth dependence of earthquake frequency-magnitude distributions in California: Implications for rupture initiation. *Journal of Geophysical Research*, *102*, 15,081–15,090. https://doi.org/10.1029/97JB01356

Muhuri, S. K., Dewers, T. A., Scott, T. E., & Reches, Z. (2003). Interseismic fault strengthening and earthquake-slip instability: Friction or cohesion? *Geology*, *31*(10), 881–884.

Nadeau, R. M., & Dolenc, D. (2005). Nonvolcanic tremors deep beneath the san andreas fault. *Science*, *307*(5708), 389–389.

Nadeau, R. M., & Guilhem, A. (2009). Nonvolcanic tremor evolution and the san simeon and parkfield, california, earthquakes. *Science*, *325*(5937), 191–193.

Nadeau, R. M., & McEvilly, T. V. (1999). Fault slip rates at depth from recurrence intervals of repeating microearthquakes. *Science*, *285*(5428), 718–721.

Obara, K. (2002). Nonvolcanic Deep Tremor Associated with Subduction in Southwest Japan. *Science*, *296*, 1679–1681. https://doi.org/10.1126/science.1070378

Obara, K., Hirose, H., Yamamizu, F., & Kasahara, K. (2004). Episodic slow slip events accompanied by non-volcanic tremors in southwest Japan subduction zone. *Geophysical Research Letters*, *31*, L23602. https://doi.org/10.1029/2004GL020848

Peng, Z., & Gomberg, J. (2010). An integrated perspective of the continuum between earthquakes and slow-slip phenomena. *Nature Geoscience*, *3*, 599–607. https://doi.org/10.1038/ngeo940

Poirier, L., Lozowski, E. P., & Thompson, R. I. (2011). Ice hardness in winter sports. *Cold Regions Science and Technology*, *67*(3), 129–134.

Press, F., & Ewing, M. (1951). Propagation of elastic waves in a floating ice sheet. *Eos, Transactions American Geophysical Union*, *32*(5), 673–678.

Rayleigh, L. (1888). On the free vibrations of an infinite plate of homogeneous isotropic elastic matter. *Proceedings of the London Mathematical Society*, *1*(1), 225–237.

Reches, Z. (1999). Mechanisms of slip nucleation during earthquakes. *Earth and Planetary Science Letters*, *170*, 475–486. https://doi.org/10.1016/S0012-821X(99)00122-3

Renard, F., Beauprêtre, S., Voisin, C., Zigone, D., Candela, T., Dysthe, D. K., & Gratier, J.-P. (2012). Strength evolution of a reactive frictional interface is controlled by the dynamics of contacts and chemical effects. *Earth and Planetary Science Letters*, *341*, 20–34.

Rice, J. R., & Ruina, A. L. (1983). Stability of Steady Frictional Slipping. *Journal of Applied Mechanics*, *50*, 343. https://doi.org/10.1115/1.3167042

Rivière, J., Lv, Z., Johnson, P. A., & Marone, C. (2018). Evolution of b-value during the seismic cycle: Insights from laboratory experiments on simulated faults. *Earth and Planetary Science Letters*, *482*, 407–413. https://doi.org/10.1016/j.epsl.2017.11.036

Rogers, G., & Dragert, H. (2003). Episodic Tremor and Slip on the Cascadia Subduction Zone: The Chatter of Silent Slip. *Science*, *300*, 1942–1943. https://doi.org/10.1126/science.1084783

Roland, E., & McGuire, J. J. (2009). Earthquake swarms on transform faults. *Geophysical Journal International*, *178*, 1677–1690.

Rosenau, M., Corbi, F., & Dominguez, S. (2017). Analogue earthquakes and seismic cycles: experimental modelling across timescales. *Solid Earth*, *8*(3), 597–635.

Roux, S., Schmittbuhl, J., Vilotte, J.-P., & Hansen, A. (1993). Some physical properties of self-affine rough surfaces. *EPL (Europhysics Letters)*, *23*, 277. https://doi.org/10.1209/0295-5075/23/4/007

Saragiotis, C. D., Hadjileontiadis, L. J., & Panas, S. M. (2002). PAI-S/K: A robust automatic seismic P phase arrival identification scheme. *IEEE Transactions on Geoscience and Remote Sensing*, *40*, 1395–1404. https://doi.org/10.1109/TGRS.2002.800438

Scholz, C. H. (1968a). The frequency-magnitude relation of microfracturing in rock and its relation to earthquakes. *Bulletin of the seismological society of America*, *58*(1), 399–415.

Scholz, C. H. (1968b). Experimental study of the fracturing process in brittle rock. *Journal of Geophysical Research*, *73*, 1447–1454.

Scholz, C. H. (1968c). Microfractures, aftershocks, and seismicity. *Bulletin of the Seismological Society of America*, *58*(3), 1117–1130.

Scholz, C. H. (1972). Crustal movements in tectonic areas. *Tectonophysics*, *14*, 201–217.

Scholz, C. H. (1998). Earthquakes and friction laws. *Nature*, *391*(6662), 37–42.

Scholz, C. H. (2002). *The Mechanics of Earthquakes and Faulting* (2 ed.). Cambridge, UK: Cambridge University Press.

Scholz, C. H. (2015). On the stress dependence of the earthquake b value. *Geophysical Research Letters*, *42*, 1399–1402. https://doi.org/10.1002/2014GL062863

Scholz, C. H., & Campos, J. (2012). The seismic coupling of subduction zones revisited. *Journal of Geophysical Research*, *117*, B05310. https://doi.org/10.1029/2011JB009003

Scholz, C. H., & Cowie, P. A. (1990). Determination of total strain from faulting using slip measurements. *Nature*, *346*, 837–839.

Schorlemmer, D., Wiemer, S., & Wyss, M. (2005). Variations in earthquake-size distribution across different stress regimes. *Nature*, *437*, 539–542. https://doi.org/10.1038/nature04094

Schulson, E. M. (2001). Brittle failure of ice. *Engineering Fracture Mechanics*, *68*(17), 1839–1887.

Schulson, E. M., & Duval, P. (2009). *Creep and Fracture of Ice* (pp. 416). Cambridge, UK: Cambridge University Press.

Schulson, E. M., & Fortt, A. L. (2012). Friction of ice on ice. *Journal of Geophysical Research*, *117*, B12204. https://doi.org/10.1029/2012JB009219

Segall, P., Desmarais, E. K., Shelly, D., Miklius, A., & Cervelli, P. (2006). Earthquakes triggered by silent slip events on Kīlauea volcano, Hawaii. *Nature*, *442*, 71–74. https://doi.org/10.1038/nature04938

Shelly, D. R. (2017). A 15 year catalog of more than 1 million low-frequency earthquakes: Tracking tremor and slip along the deep San Andreas Fault. *Journal of Geophysical Research: Solid Earth*, *122*, 3739–3753. https://doi.org/10.1002/2017JB014047

Shelly, D. R., Beroza, G. C., & Ide, S. (2007). Non-volcanic tremor and low-frequency earthquake swarms. *Nature*, *446*, 305–307.

Shelly, D. R., Beroza, G. C., Ide, S., Nakamula, S., & their relationship to episodic tremor and slip (2006). Low-frequency earthquakes in Shikoku, Japan. *Nature*, *442*, 188–191. https://doi.org/10.1038/nature04931

Shen, Z.-K., Jackson, D. D., Feng, Y., Cline, M., Kim, M., Fang, P., & Bock, Y. (1994). Postseismic deformation following the landers earthquake, california, 28 june 1992. *Bulletin of the Seismological Society of America*, *84*(3), 780–791.

Staudenmaier, N., Tormann, T., Edwards, B., Mignan, A., & Wiemer, S. (2019). The frequency-size scaling of non-volcanic tremors beneath the san andreas fault at parkfield: Possible implications for seismic energy release. *Earth and Planetary Science Letters*, *516*, 77–107.

Sykes, L. R. (1970). Earthquake swarms and sea-floor spreading. *Journal of Geophysical Research*, *75*, 6598–6611.

Tadokoro, K., & Ando, M. (2002). Evidence for rapid fault healing derived from temporal changes in s wave splitting. *Geophysical Research Letters*, *29*(4), 1047. https://doi.org/10.1029/2001GL013644

Tadokoro, K., Ando, M., & Umeda, Y. (1999). S wave splitting in the aftershock region of the 1995 Hyogo-ken Nanbu earthquake. *Journal of Geophysical Research*, *104*, 981–991. https://doi.org/10.1029/1998JB900024

Tenthorey, E., & Cox, S. F. (2006). Cohesive strengthening of fault zones during the interseismic period: An experimental study. *Journal of Geophysical Research*, *111*, B09202. https://doi.org/10.1029/2005JB004122

Thomas, A. M., Beeler, N. M., Bletery, Q., Burgmann, R., & Shelly, D. R. (2018). Using Low-Frequency Earthquake Families on the San Andreas Fault as Deep Creepmeters. *Journal of Geophysical Research: Solid Earth*, *123*, 457–475. https://doi.org/10.1002/2017JB014404

Uchida, N., Matsuzawa, T., Hasegawa, A., & Igarashi, T. (2003). Interplate quasi-static slip off sanriku, ne japan, estimated from repeating earthquakes. *Geophysical Research Letters*, *30*(15), 1801. https://doi.org/10.1029/2003GL017452

Utsu, T. (2002). Statistical features of seismicity, *International Handbook of Earthquake and Engineering Seismology* (pp. 719–732). Amsterdam: Academic Press.

Vanderkulk, W., Rosen, F., & Lorenz, S. (1965). Large aperture seismic array signal processing study (*IBM Final Report*): ARPA Contract Number SD-296.

Wech, A. G., & Creager, K. C. (2007). Cascadia tremor polarization evidence for plate interface slip. *Geophysical Research Letters*, *34*, L22306. https://doi.org/10.1029/2007GL031167

Weiss, J., Pellisier, V., Marsan, D., Arnaud, L., & Renard, F. (2016). Cohesion versus friction in controlling the long-term strength of self-healing experimental fault. *Journal of Geophysical Research: Solid Earth*, *121*, 8523–8547. https://doi.org/10.1002/2016JB013110

Weiss, J., & Schulson, E. M. (2000). Grain-boundary sliding and crack nucleation in ice. *Philosophical Magazine, Part A*, *80*, 279–300. https://doi.org/10.1080/014186100250859

Wiemer, S., & Katsumata, K. (1999). Spatial variability of seismicity parameters in aftershock zones. *Journal of Geophysical Research*, *104*, 13.

Wiemer, S., McNutt, S. R., & Wyss, M. (1998). Temporal and three-dimensional spatial analyses of the frequency-magnitude distribution near long valley caldera, california. *Geophysical Journal International*, *134*, 409–421.

Wiemer, S., & Wyss, M. (2002). Mapping spatial variability of the frequency-magnitude distribution of earthquakes. *Advances in Geophysics*, *45*, 259.